Monthly Notices
of the
ROYAL ASTRONOMICAL SOCIETY

MNRAS **494,** 5882–5901 (2020)
Advance Access publication 2020 May 02

doi:10.1093/mnras/staa1133

Luminous Type II supernovae for their low expansion velocities

Ó. Rodríguez,[1,2,3★] G. Pignata,[1,2] J. P. Anderson,[4] T. J. Moriya,[5,6] A. Clocchiatti,[2,7] F. Förster,[2,8] J. L. Prieto,[2,9] M. M. Phillips,[10] C. R. Burns,[11] C. Contreras,[10] G. Folatelli,[12,13,14] C. P. Gutiérrez,[15] M. Hamuy,[2,16] N. I. Morrell,[10] M. D. Stritzinger,[17] N. B. Suntzeff,[18] S. Benetti,[19] E. Cappellaro,[19] N. Elias-Rosa,[19] A. Pastorello,[19] M. Turatto,[19] J. Maza,[16] R. Antezana,[16] R. Cartier,[20] L. González,[16] J. B. Haislip,[21] V. Kouprianov,[21] P. López,[14] S. Marchi-Lasch[16] and D. Reichart[21]

Affiliations are listed at the end of the paper

Accepted 2020 April 21. Received 2020 April 16; in original form 2019 October 7

ABSTRACT

We present optical and near-infrared data of three Type II supernovae (SNe II), SN 2008bm, SN 2009aj, and SN 2009au. These SNe display the following common characteristics: signs of early interaction of the ejecta with circumstellar material (CSM), blue $B - V$ colours, weakness of metal lines, low expansion velocities, and V-band absolute magnitudes 2–3 mag brighter than those expected for normal SNe II based on their expansion velocities. Two more SNe reported in the literature (SN 1983K and LSQ13fn) share properties similar to our sample. Analysing this set of five SNe II, which are luminous for their low expansion velocities (LLEV), we find that their properties can be reproduced assuming ejecta–CSM interaction that lasts between 4 and 11 weeks post-explosion. The contribution of this interaction to the radiation field seems to be the dominant component determining the observed weakness of metal lines in the spectra rather than the progenitor metallicity. Based on hydrodynamic simulations, we find that the interaction of the ejecta with a CSM of $\sim$3.6 $M_{\odot}$ can reproduce the light curves and expansion velocities of SN 2009aj. Using data collected by the Chilean Automatic Supernova Search, we estimate an upper limit for the LLEV SNe II fraction to be 2–4 per cent of all normal SNe II. With the current data set, it is not clear whether the LLEV events are a separated class of SNe II with a different progenitor system, or whether they are the extreme of a continuum mediated by CSM interaction with the rest of the normal SN II population.

Key words: circumstellar matter – supernovae: general – supernovae: individual: SN 1983K – supernovae: individual: SN 2008bm – supernovae: individual: SN 2009aj – supernovae: individual: SN 2009au – supernovae: individual: LSQ13fn.

1 INTRODUCTION

Type II supernovae (SNe II; Minkowski 1941) are the final stage of the evolution of stars with an initial mass >8 $M_{\odot}$, which retain a significant fraction of hydrogen in their envelopes at the moment of the collapse of their iron cores. Among SNe II, three special sub-types have been identified based on their photometric and spectroscopic characteristics: those showing hydrogen in early spectra that soon disappear (SNe IIb; Woosley et al. 1987; Filippenko 1988), those having light curves similar to SN 1987A (1987A-like SNe, e.g. Hamuy et al. 1988), and those showing narrow hydrogen emission lines in the spectra due to the interaction of the ejecta with a circumstellar material (CSM) (SNe IIn; Schlegel 1990). For the rest of SNe II (77 per cent; Shivvers et al. 2017, which show a range in luminosity decline rates), we will refer as normal SNe II.

Among SNe IIn, there are some events that after 25–50 d past explosion start to look similar to normal SNe II with broad P-Cygni profiles, but with bluer colours (hereafter SNe IIn/II, e.g. SN 1979C, Balinskaia, Bychkov & Neizvestnyi 1980; Branch et al. 1981; de Vaucouleurs et al. 1981; SN 1998S, Fassia et al. 2000, 2001; SN 2007pk, Inserra et al. 2013; SN 2008fq, Taddia et al. 2013; Faran et al. 2014; PTF11iqb, Smith et al. 2015; SN 2013fc, Kangas et al. 2016). On the other hand, Smith et al. (2015) suggested that some normal SNe II could be classified as SNe IIn if the

★ E-mail: olrodrig@gmail.com

classification spectra are taken at epochs early enough to detect the interaction of the ejecta with the CSM generated by progenitors with dense winds.

Recently, it has been shown that the presence of CSM around progenitors of normal SNe II seems to be ubiquitous (Förster et al. 2018). In fact, the ejecta–CSM interaction in normal SNe II, previously detected only in few cases (e.g. SN 2006bp; Quimby et al. 2007), now is confirmed in many cases by the detection of narrow hydrogen emission lines in very early-time spectroscopy (also called "flash spectroscopy", Khazov et al. 2016; Yaron et al. 2017). The effect of this early ejecta–CSM interaction over the radiation field is also inferred from the light curve modelling (Moriya et al. 2011; Das & Ray 2017; Morozova, Piro & Valenti 2017, 2018; Förster et al. 2018) and, more recently, from the simultaneous modelling of light curves and spectra (Hillier & Dessart 2019).

With the increasing number of discovered SNe II, more rare events are being revealed. An example of this is LSQ13fn (Polshaw et al. 2016), an SN II that shares some of the properties seen on SNe IIn/II (e.g. early ejecta–CSM interaction, blue colours, and high luminosities) but with two additional characteristics: (1) weakness of metal lines in the spectra, and (2) low expansion velocities, with values between the subluminous SN II 2005cs (Pastorello et al. 2006, 2009), and the archetypal SN II 1999em (Hamuy et al. 2001; Leonard et al. 2002; Elmhamdi et al. 2003), but having a luminosity comparable to the moderately luminous SN II 2004et (Sahu et al. 2006; Maguire et al. 2010). In addition to LSQ13fn, SN 1983K was also reported showing some of the aforementioned characteristics (Niemela, Ruiz & Phillips 1985; Phillips et al. 1990). SN 1983K and LSQ13fn, being more luminous than the expected from their expansion velocities, do not fall on the luminosity–expansion velocity relation found by Hamuy & Pinto (2002) for normal SNe II. Polshaw et al. (2016) suggested a combined effect of a residual thermal energy from the early ejecta–CSM interaction, a low metallicity, and a large radius of the progenitor to explain the peculiarities seen in LSQ13fn. In this work, we present optical and near-infrared (near-IR) data of SN 2008bm, SN 2009aj, and SN 2009au, which show similar properties to those seen in SN 1983K and LSQ13fn. Throughout this paper, we identify this sample of SNe II using the acronym luminous for their low expansion velocities (LLEV) SNe II.

The paper is organized as follows. In Section 2, we present the relevant information on our SN data set and their host galaxies. Photometry along with the description of the data reduction is presented in Section 3. In Sections 4 and 5, we contrast the properties of the LLEV SNe II with those of other SNe II. A possible scenario that could explain the peculiar characteristics seen in the LLEV SNe II is discussed in Section 6. We also present an estimation of the fraction of LLEV SNe II with respect to normal SNe II in Section 6.3 and their impact on the use of normal SNe II as distance indicators in Section 6.4. Finally, our conclusions are summarized in Section 7.

2 SUPERNOVAE AND HOST GALAXIES

In Table 1, we list the main parameters of the LLEV SNe II in our set and their host galaxies. Throughout this work, we assume the extinction curve given by Fitzpatrick (1999) with $R_V = 3.1$. To compute distances from recessional redshifts, we assume $H_0 = 73$ km s^{-1} Mpc^{-1}, $\Omega_m = 0.27$, and $\Omega_\Lambda = 0.73$. To estimate the error in distances due to peculiar velocities, we include a velocity dispersion of 382 km s^{-1} (Wang et al. 2006).

2.1 SN 2008bm

SN 2008bm was discovered in the galaxy CGCG 71–101 on 2008 March 29.3 UT (Drake et al. 2008) by the Catalina Real-time Transient Survey (CRTS; Drake et al. 2009). The SN is also present on images taken on January 31.5 UT. The last non-detection was on January 11.5 UT; therefore, the explosion epoch is constrained to occur at MJD 54486.5 ± 10.0,[1] which is 67.8 d before the discovery. The event was classified as an SN IIn a couple of months past explosion based on a spectrum obtained on April 7.1 UT. Stritzinger & Morrell (2008) initially classified SN 2008bm as an SN IIn, while the latter spectra reported by Gutiérrez et al. (2017a, hereafter G17) show clear Balmer absorption lines, typically seen in normal SNe II. No radio detection was obtained in the 8.46-GHz band at the SN position on December 07.7 UT (Chandra & Soderberg 2008).

CGCG 71–101 has a recessional velocity of 9875 km s^{-1} (NED[2]), which translates into a distance modulus of 35.66 ± 0.08 mag. No Na I D absorption at the redshift of the host galaxy was detected in the SN spectra, indicating a negligible host galaxy reddening ($E^{\rm host}_{B-V} = 0.00 \pm 0.03$ mag, Anderson et al. 2014b, hereafter A14). SN 2008bm is located at a projected distance of 9.3 ± 0.3 kpc from the center of the apparently nearly face-on host galaxy, which is consistent with the low reddening scenario.

2.2 SN 2009aj

SN 2009aj was discovered in the galaxy ESO 221–G18 on 2009 February 24.3 UT (Pignata et al. 2009b) during the Chilean Automatic Supernova Search (CHASE; Pignata et al. 2009a). Nothing was visible at the SN position on February 11.2 UT, therefore the explosion is constrained to occur at MJD 54879.8 ± 6.5 (i.e. 6.5 d before the discovery). The event was classified by Stritzinger et al. (2009) as an SN II around maximum and reminiscent of SN 1983K.

We do not detect the presence of Na I D at the redshift of the host galaxy in the SN spectra. In this case, we assume zero reddening with an error corresponding to the 3σ upper limit of the Na I D pseudo-equivalent width (pEW) non-detection. Using the relation of Poznanski, Prochaska & Bloom (2012),[3] we obtain $E^{\rm host}_{B-V} = 0.00 \pm 0.02$ mag, which we adopt as the host galaxy colour excess. ESO 221–G18 has a recessional velocity corrected for the infall of the Local Group toward the Virgo cluster and the Great Attractor of 4380 ± 112 km s^{-1} (NED), which translates into a distance modulus of 33.89 ± 0.20 mag.

2.3 SN 2009au

SN 2009au was discovered in the galaxy ESO 443–G21 on 2009 March 11.2 UT (Pignata et al. 2009c) by the CHASE survey. Nothing was visible at the SN position on March 3.2 UT, therefore the explosion epoch is constrained to occur at MJD 54897.2 ± 4.0 (i.e. 4 d before the discovery). The event appeared to be a young SN IIn soon after the explosion (Stritzinger et al. 2009), however, the later spectra (see G17) show clear Balmer absorption features. No radio detection was obtained at the SN position in the 8.46-GHz band on December 13.6 UT (Chandra & Soderberg 2009).

[1] We assume the explosion epoch as the mid-point of the range between the last non-detection and the first detection of the SN, with the error (not normal but uniform) being half the range.
[2] NASA/IPAC Extragalactic Database (https://ned.ipac.caltech.edu/).
[3] Where, as noted by Phillips et al. (2013), the error around the log (E_{B-V}) relation is of 0.30 dex.

Table 1. SN and host galaxy parameters of the LLEV SN II sample.

SN data	1983K	2008bm	2009aj	2009au	LSQ13fn
RA (J2000.0)	12:46:36.41	13:02:58.78	13:56:45.33	12:59:46.00	11:51:17.29
Dec. (J2000.0)	−8:21:21.9	+10:30:27.0	−48:29:36.2	−29:36:07.5	−29:36:41.10
Host galaxy	NGC 4699	CGCG 71–101	ESO 221–G18	ESO 443–G21	LEDA 727284
Host type[a]	SAB(rs)b	Sc	Sa?	Scd	Sa[e]
Distance modulus (mag)	31.50 ± 0.35	35.66 ± 0.08	33.89 ± 0.20	33.31 ± 0.22	37.21 ± 0.05
$E^{\rm MW}_{B-V}$ (mag)[b]	0.015 ± 0.002	0.022 ± 0.003	0.124 ± 0.020	0.079 ± 0.013	0.054 ± 0.009
$E^{\rm host}_{B-V}$ (mag)	0.0[d]	0.00 ± 0.03	0.00 ± 0.02	0.35 ± 0.17	0.0[e]
Explosion epoch (MJD)	45490.1 ± 1.0	54486.5 ± 10.0	54879.8 ± 6.5	54897.2 ± 4.0	56299.2 ± 1.0
SN heliocentric velocity (km s^{-1})	1394 ± 162	9628 ± 25	2883 ± 162	2875 ± 30	18900 ± 300[e]
12+log(O/H) (dex)[c]	8.55†	8.33 ± 0.02⋆	8.29 ± 0.03⋆	8.56 ± 0.03⋆	<8.50 ± 0.16⊗
s_2 (mag (100 d)$^{-1}$)	0.73 ± 0.10	2.56 ± 0.21	0.80 ± 0.02	3.06 ± 0.02	0.86 ± 0.10
$M_V^{\rm max}$ (mag)	−18.83 ± 0.36	−18.40 ± 0.18	−18.81 ± 0.21	−17.55 ± 0.58	−17.95 ± 0.21
$M_V^{\rm 50d}$ (mag)	−18.43 ± 0.35	−18.33 ± 0.15	−17.81 ± 0.22	−16.54 ± 0.59	−17.33 ± 0.07
^{56}Ni mass (M$_\odot$)	0.056 ± 0.018	>0.015 ± 0.005	>0.043 ± 0.010	–	>0.018 ± 0.005
$(B-V)_{\rm 50d}$ (mag)	0.30 ± 0.03	<0.12 ± 0.03	0.41 ± 0.05	0.48 ± 0.15	0.34 ± 0.11
pEW(Fe II λ5018)$_{\rm 50d}$ (Å)	3.46 ± 0.22	<8.00 ± 3.00	9.02 ± 0.90	14.65 ± 2.63	9.00 ± 2.20
$v^{\rm 50d}_{\rm FeII}$ (km s^{-1})	2331 ± 189	1684 ± 110	2336 ± 181	1549 ± 40	2320 ± 345

[a]From NED, unless otherwise noted.
[b]Galactic colour excesses from Schlafly & Finkbeiner (2011), with a statistical error of 16 per cent (Schlegel, Finkbeiner & Davis 1998).
[c]Oxygen abundances, in the N2 calibration of Marino et al. (2013), measured by Kuncarayakti et al. (2018) (†), Anderson et al. (2016) (⋆), or Polshaw et al. (2016) (⊗). The latter is a recalibration of the original value reported in the N2 calibration of Pettini & Pagel (2004).
[d]Value from Niemela et al. (1985).
[e]Value from Polshaw et al. (2016).

The distance modulus to ESO 443–G21 is estimated using the Tully–Fisher relation to be 33.44 ± 0.45 mag (Tully, Courtois & Sorce 2016). In addition, ESO 443–G21 is a member of the galaxy group HDCE 754 (Crook et al. 2007), which has a recessional velocity corrected for Virgo infall of 3287 km s^{-1} (NED), corresponding to a distance modulus of 33.27 ± 0.25 mag. We adopt the weighted mean of these values (μ = 33.31 ± 0.22 mag) as the distance to ESO 443–G21.

SN 2009au is located at a projected distance of 1.7 ± 0.1 kpc from the center of its edge-on host galaxy, so the SN could be affected by a high amount of extinction. We measured a Na I D pEW of 1.33 ± 0.21 Å at the redshift of the host galaxy in the SN spectra. However, the Na I D pEW becomes insensitive to estimate reddening for pEW > 1.0 Å (Phillips et al. 2013). Despite the above, we can estimate a lower limit for the $E^{\rm host}_{B-V}$ value as the saturation point (pEW = 1.0 Å) in the Poznanski et al. (2012) relation ($E^{\rm host}_{B-V} > 0.21 \pm 0.14$ mag). On the other hand, matching the $B-V$ colour curve of SN 2009au to the rest of LLEV SNe II, we obtain $E^{\rm host}_{B-V} = 0.35 \pm 0.17$ mag, which is consistent with the previous lower limit. We adopt the colour excess from the $B-V$ colour match as the $E^{\rm host}_{B-V}$ value for SN 2009au.

3 OBSERVATIONAL MATERIAL

3.1 Photometric data

Optical and near-IR images of SN 2008bm, SN 2009aj, and SN 2009au were obtained over the course of the Carnegie Supernova Project I (CSP-I; Hamuy et al. 2006). Johnson *BV* and Sloan *ugri* images were obtained mostly with the 1-m Swope telescope at Las Campanas Observatory (LCO), while near-IR *YJH* images were obtained with both the 1-m Swope and the LCO 2.5-m du Pont telescope. The CSP-I data reduction is described in Contreras et al. (2010) and Krisciunas et al. (2017).

In addition, Johnson–Kron–Cousins *UBVRI* and Sloan *griz* images of SN 2009aj and SN 2009au were also obtained with the 41-cm Panchromatic Robotic Optical Monitoring and Polarimetry Telescopes (PROMPT; Reichart et al. 2005) at Cerro Tololo inter-American Observatory (CTIO), as part of the CHASE follow-up program. We also include *BVRI* images of SN 2009au obtained with the SMARTS 1.3-m telescope at CTIO, equipped with the A Novel Dual Imaging Camera (ANDICAM).[4] Data reduction includes bias subtraction, overscan correction, flat-field correction, cosmic-ray rejection, and image combination.

As part of the CSP-I and CHASE programs, images of the SNe host galaxies 1.5–4.0 yr after the SN explosion were obtained in order to remove the host galaxy contamination. In the case of the ANDICAM images of SN 2009au, to construct a template for each filter, we selected the earliest images of the SN field obtained under good observing conditions with such camera. Then, using the SNOoPY[5] package, we removed the SN flux. Such templates were then subtracted from the rest of the images acquired with ANDICAM. Instrumental magnitudes were measured using the point spread function (PSF) technique. Final magnitudes were computed with respect to a local sequence of stars (Tables A1–A6), which are calibrated using Landolt (1992) *UBVRI*, Smith et al. (2002) *ugriz*, and Persson et al. (1998) *JHK* standard stars (*J*- and *K*-band observations were used to derive *Y*-band magnitudes of the standard stars, see Hamuy et al. 2006).

Tables A7–A9 list the standard system photometry of SN 2008bm, SN 2009aj, and SN 2009au, while Fig. 1 shows their optical and near-IR light curves. Systematic differences between the CSP-I and CHASE *BVgri* photometry, CSP-I and ANDICAM *BV* photometry, and CHASE and ANDICAM *RI* photometry are, on average, lower than 0.02 mag. We stress the fact that the

[4]Images are available on the NOAO science archive (http://archive1.dm.noao.edu/).
[5]SNOoPy is a package for SN photometry using PSF fitting and/or template subtraction developed by E. Cappellaro. A package description can be found at http://sngroup.oapd.inaf.it/snoopy.html

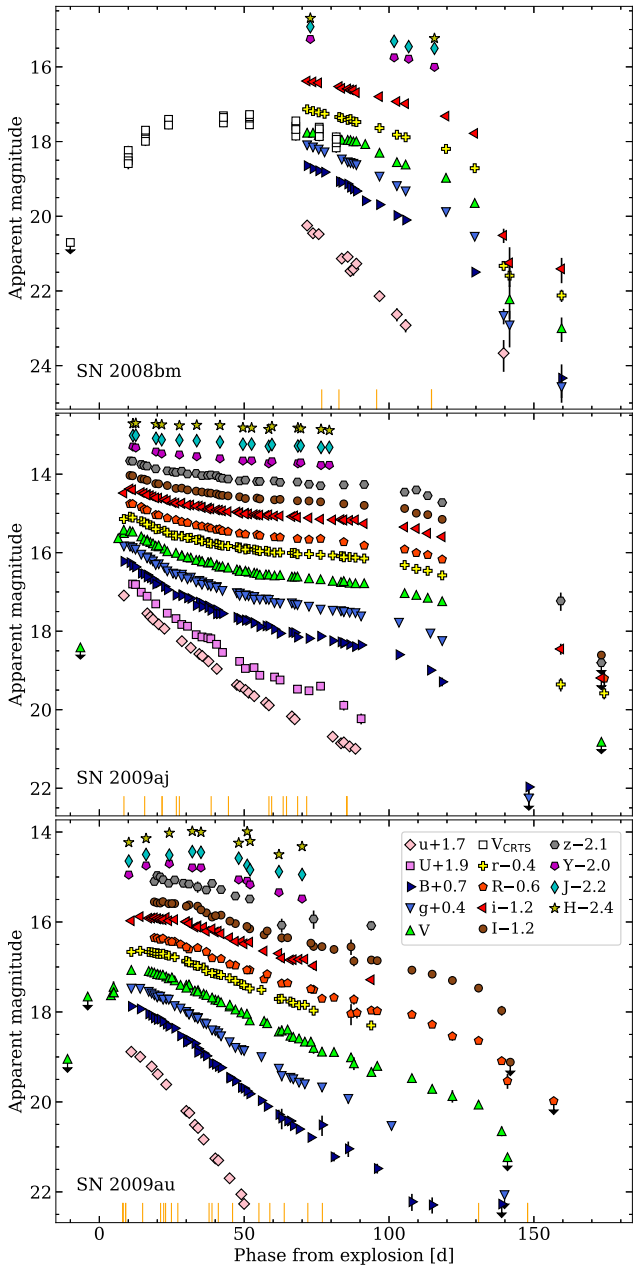

Figure 1. Light curves of SN 2008bm (top panel), SN 2009aj (middle panel), and SN 2009au (bottom panel). Bands and magnitude shifts with respect to the original values are quoted in the legend. Arrows indicate upper limits. Orange ticks mark the epochs of the spectroscopy. For SN 2008bm, we also plot the CRTS photometry.

photometry obtained with the SMARTS 1.3 m and PROMPT telescopes was calibrated using the magnitudes of the CSP-I local sequences.

In the analysis, we include the unfiltered photometry transformed into *V*-band magnitudes (V_{CRTS}) of SN 2008bm obtained by the CRTS.[6] We note that the V_{CRTS} photometry lies very close to our *r*-band photometry in the phase interval where the light curves overlap. In order to reach, a better agreement between the V_{CRTS} and the filtered *V*-band photometry, we add 0.26 mag to the V_{CRTS} magnitudes, which is the average $V - r$ colour at 50 d since explosion we obtained for SN 2009aj and LSQ13fn.

[6]Available on http://nesssi.cacr.caltech.edu/DataRelease/CRTS-I_transients.html

3.2 Spectroscopic data

Optical spectra of SN 2009au were obtained with telescopes and instruments listed in Table A10. Data reduction includes bias subtraction, flat-field correction, wavelength calibration, one-dimensional spectrum extraction and sky subtraction, and flux calibration. The left-hand side of Fig. A1 shows the optical spectral evolution of SN 2009au.

We also obtained near-IR spectra of SN 2009aj with telescopes and instruments listed in Table A11. Data reduction includes the subtraction of the pairs of images to remove the sky background, images combination, wavelength calibration, one-dimensional spectrum extraction, telluric correction, and flux calibration. The right-hand side of Fig. A1 shows the near-IR spectral evolution of SN 2009aj.

In the analysis, we include the optical spectroscopy for SN 2008bm, SN 2009aj, and SN 2009au, which was obtained by the CSP-I and already published in G17.

3.3 Sample of supernovae

In addition to SN 2008bm, SN 2009aj, and SN 2009au, we include SN 1983K (Niemela et al. 1985; Phillips et al. 1990) and LSQ13fn (Polshaw et al. 2016) into the analysis, given the similarity of their photometric and spectral properties (see Section 4 and 5). SN 1983K was discovered in NGC 4699 on 1983 June 6.1 UT (Maza, Wischnjewsky & Gonzalez 1983) at 17.1 mag (Phillips et al. 1990). There is no information about the last non-detection. However, the SN was at 13.3 mag on June 10.1 UT (Phillips et al. 1990), which indicates that the SN was discovered close to the explosion. Fitting a quadratic polynomial to the *B*-band rise photometry, we obtain the explosion epoch to be MJD 45490.1 ± 1.0 (i.e. 1 d before the discovery). The distance modulus to NGC 4699 is estimated with the Tully–Fisher relation to be 31.45 ± 0.45 mag (Tully et al. 2016). In addition, NGC 4699 is a member of the galaxy group HDCE 740 (Crook et al. 2007), which has a recessional velocity corrected for Virgo infall of 1506 km s^{-1} (NED), corresponding to a distance modulus of 31.57 ± 0.55 mag. We adopt the weighted mean (μ = 31.50 ± 0.35 mag) as the distance to NGC 4699. LSQ13fn was discovered in LEDA 727284 on 2013 January 10.2 UT by the La Silla-Quest Variability Survey (Baltay et al. 2013), which also obtained early-time photometry. The first detection was on January 8.2 UT, while the last non-detection was on January 6.2 UT, so the explosion is constrained to occur at MJD 56299.2 ± 1.0 (i.e. 3 d before the discovery). Using the redshift given in Polshaw et al. (2016) and the cosmic microwave background dipole model of Fixsen et al. (1996), we compute a recessional velocity of 19225 ± 300 km s^{-1} for LEDA 727284, corresponding to a distance modulus of 37.21 ± 0.05 mag. The main parameters for SN 1983K, LSQ13fn, and their host galaxies are summarized in Table 1.

4 PHOTOMETRIC PROPERTIES

In this section, we compare photometric properties of the LLEV SNe II with those of other SNe II.

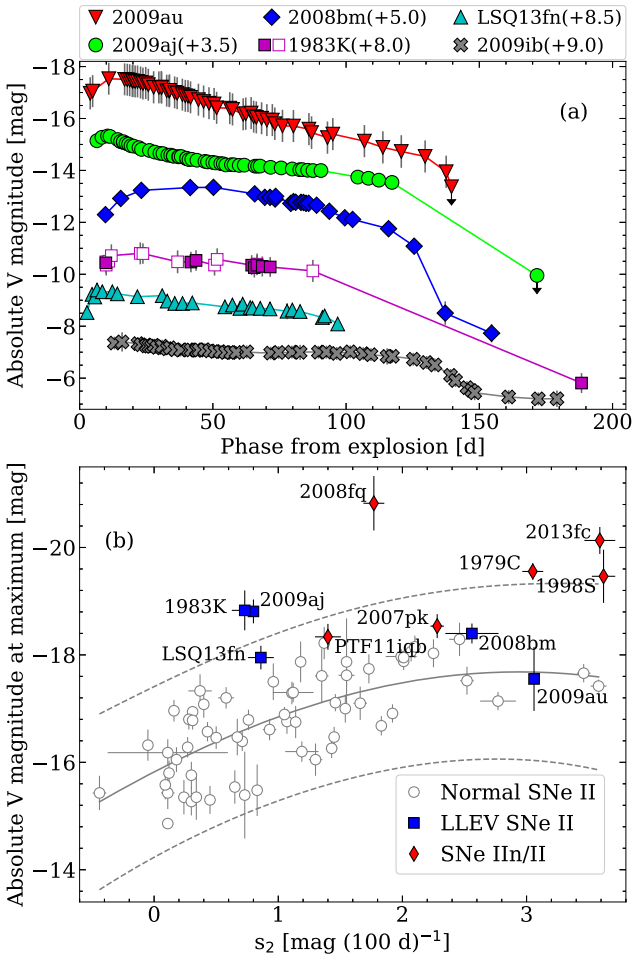

Figure 2. (a) Absolute V-band light curves of the LLEV SNe II in our set (coloured symbols), and of the normal SN II 2009ib (grey crosses). For clarity, we averaged photometric points into 2-h bins, and applied and offset to magnitudes (indicated in parentheses). Arrows indicate upper limits. (b) Absolute V-band magnitude at maximum versus V-band decline rate during the plateau, showing the LLEV SNe II in our set (blue squares), the normal SNe II in the A14 sample corrected for $E^{\rm host}_{B-V}$ (empty circles), and the SNe IIn/II from the literature (red diamonds). The solid line corresponds to the Gaussian process fit, where dashed lines indicate the 3σ error around the fit.

4.1 *V*-band light curves

Fig. 2(a) shows the absolute V-band light curves of the LLEV SNe II in our set. We note that the length of the photospheric phase (also called optically thick phase duration, OPTd) of SN 2008bm and SN 2009aj is about 120 d, and of about 130 d for SN 2009au. These values are comparable to that of SNe II 2004er (120 d; A14) and 2009ib (Takáts et al. 2015, grey crosses), which are among the normal SNe II with longest plateau.

Analysing a set of 116 SN II V-band light curves, A14 found a correlation between the absolute V-band magnitude at maximum ($M^{\rm max}_V$) and the decline rate of the second, shallower slope in the light curve (s_2), which suggests a continuum in the normal SN II population in this parameter space. Similar peak magnitude-decline rate correlations were also obtained by Sanders et al. (2015), Galbany et al. (2016), and Valenti et al. (2016).

For SN 2008bm, SN 2009aj, SN 2009au, and LSQ13fn, we have V-band photometry around the maximum light. Therefore, we can check if such correlation holds also for LLEV SNe II. In the case of SN 1983K, the V-band light curve (purple filled squares) is less sampled than the B-band one (see fig. 3 of Phillips et al. 1990), and the maximum light (observed in the B band) in the V band is missed. To estimate the V-band photometry around the maximum, we interpolate the $B-V$ colour (which is monotonically increasing, see Section 4.3) to the epochs of the B-band photometry without V-band measurements (t^*), and then we compute $V_{t^*} = B_{t^*} - (B-V)_{t^*}$ (purple empty squares). To estimate the V-band maximum of our LLEV SNe II, we fit a fourth-order polynomial to the photometry close in time to the brightest point. To estimate s_2, we fit a straight line to the V-band light curve during the plateau phase (for more details, see A14). Values of $M^{\rm max}_V$ and s_2 for the LLEV SNe II set are listed in Table 1.

Fig. 2(b) shows the normal SNe II in the A14 sample[7] (empty circles; where values are from Table 6 of A14) in the $M^{\rm max}_V$ versus s_2 space, where we remove those SNe without estimation of $E^{\rm host}_{B-V}$. To characterize the distribution of the A14 sample in this space, we perform a Gaussian process fit (solid line), where the dashed lines indicate the $\pm 3\sigma$ limits. In the figure, we plot the LLEV SNe II as blue squares. We see that they have $M^{\rm max}_V \lesssim -17.5$ mag, where SN 2008bm and SN 2009au are fast decliners, while for SN 1983K, SN 2009aj, and LSQ13fn the decline rate is lower, indicating that LLEV SNe II seems not to be connected to a particular light curve decline rate. In addition, we see that SN 2008bm, SN 2009au, and LSQ13fn are within 3σ limit, while SN 1983K and SN 2009aj are outliers in the distribution, i.e. they are significantly brighter than what would be implied from their s_2 decline rates. In the figure, we also plot the SNe IIn/II (red diamonds) that we found in the literature (the set and main properties are listed in Table A12). We see that the LLEV SNe II tend to have lower decline rates than SNe IIn/II.

The case of SN 2009au is special. Its OPTd and s_2 values are not common in normal SNe II, where faster decliners have also shorter OPTd (see e.g. fig. 12 in A14). Performing radiation hydrodynamics simulations, Hillier & Dessart (2019) showed that the ejecta–CSM interaction scenario could produce fast decliners with an OPTd similar to slow decliners. Based on the latter, we suggest that the characteristics of the V-band light curve of SN 2009au are consequence of the interaction of its ejecta with a CSM.

4.2 Pseudo-bolometric light curves

To compute pseudo-bolometric light curves, we proceed as follows: (1) we convert broad-band magnitudes into monochromatic fluxes (f_x), associated to their respective effective wavelengths (l_x). For a fair comparison with other SNe II in the literature, we use *BVRI* and *gri* magnitudes. (2) For each photometric epoch, we perform linear interpolations between the (l_x, f_x) points, which we adopt as the spectral energy distribution (SED). (3) We correct the SED for redshift and colour excess, and then we integrate it from 4200 to 7500 Å (which is a wavelength range covered by the filters). (4) We convert the integrated flux into luminosity using the corresponding SN distance.

The top part of Fig. 3 shows the *BVRI* pseudo-bolometric light curves of the LLEV SNe II in our sample, except SN 1983K for which the photometry in the necessary bands is not available.

[7]We remove SN 2008bm and SN 2009au from the A14 sample since they are in our LLEV SN II sample.

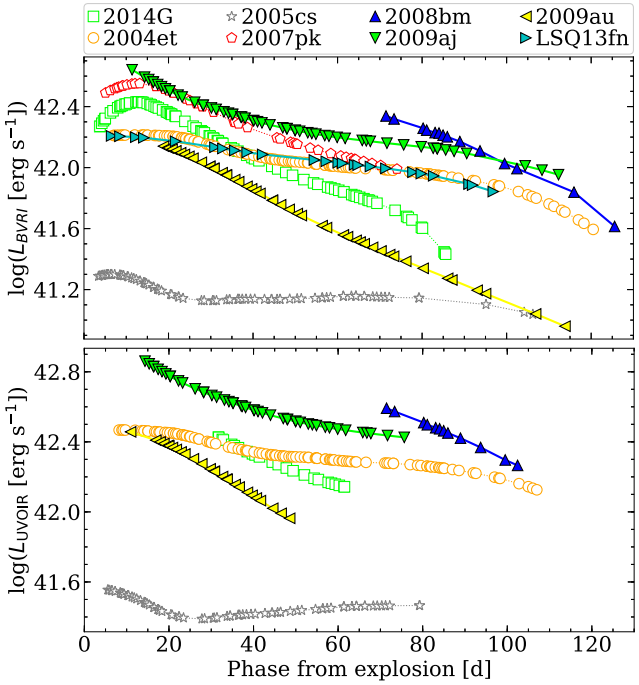

Figure 3. *BVRI* (top panel) and UVOIR (bottom panel) pseudo-bolometric light curves of the LLEV SNe II in our set (filled symbols) and a selection of SNe II that share some of the properties seen in LLEV SNe II (empty symbols).

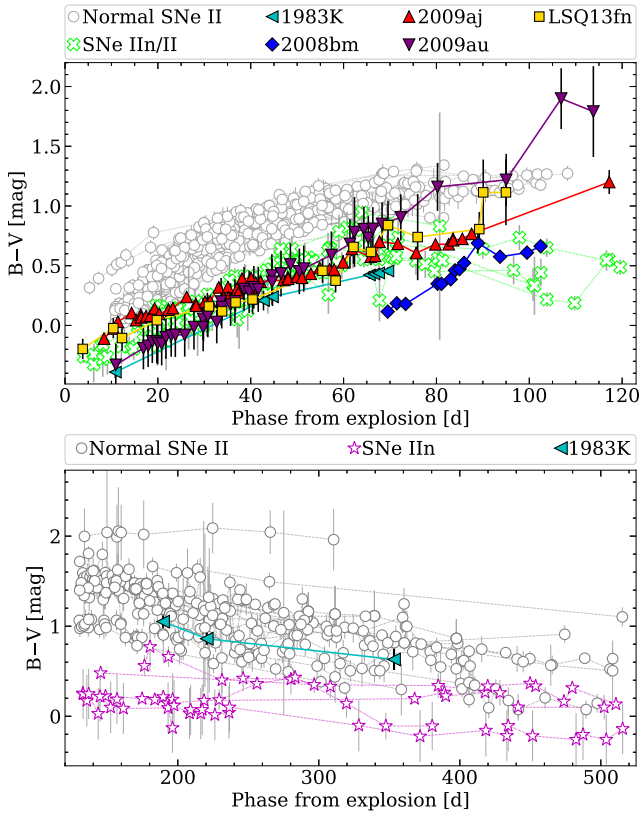

Figure 4. Evolution of the $B - V$ colour, corrected for $E^{\rm host}_{B-V}$. Top panel: during the first 120 d since explosion of the LLEV SNe II in our set (filled symbols) compared with the normal SNe II in the D18 sample (empty circles). Bottom panel: during the late-time phase of SN 1983K (filled triangle) and of normal SNe II from the literature with the *B*- and *V*-band photometry during 190–350 d since explosion (empty circles). We also include SNe IIn/II (top panel, green crosses) and SNe IIn (bottom panel, magenta stars) to depict the effect of the ejecta–CSM interaction over the $B - V$ colour.

For comparison, we also compute the *BVRI* pseudo-bolometric light curves for a selection of SNe II from the literature that share some of the properties observed in our LLEV SN II sample: normal SNe II 2014G (Bose et al. 2016; Terreran et al. 2016) and SN 2004et, which have decline rates similar to SN 2008bm and SN 2009au, and to SN 2009aj and LSQ13fn, respectively; the SN IIn/II 2007pk; and the subluminous SN II 2005cs, which has low expansion velocities (see Section 5.3). We see that SN 2008bm and SN 2009aj have luminosities higher than SNe II with a similar decline rate, confirming the result obtained in Fig. 2(b), where the luminosity of SN 2009aj is comparable to those of the SN 2007pk at epochs earlier than 40 d since explosion. After that, the evolution of the SN 2009aj luminosity is similar to that of SN 2004et, though brighter. SN 2009au is less luminous than SN 2014G in all the phase range reported in the plot, with a luminosity at maximum light similar to SN 2004et, and similar to SN 2005cs at 100 d. LSQ13fn, as reported by Polshaw et al. (2016), has a luminosity similar to SN 2004et. We also compute the pseudo-bolometric light curve using ultraviolet, optical, and near-IR (UVOIR) photometry, from *u*/*U*- up to *H*-band (3600–16500 Å, bottom part of Fig. 3). We find that SN 2008bm and SN 2009aj are not only brighter in the optical (top part of Fig. 3), but also in the UVOIR wavelength range.

4.3 Colour evolution

Normal SNe II are found to form a continuum population in observed colours, showing a large diversity at all epochs. While there are some (red) normal SNe II that clearly show the effects of strong host galaxy reddening, most of the colour dispersion apparently arises from intrinsic colour differences between normal SNe II (de Jaeger et al. 2018, hereafter D18).

The top part of Fig. 4 shows the $B - V$ colour curves of the normal SNe II analysed in D18[8] (empty circles) and corrected for $E^{\rm host}_{B-V}$ (using values of A14), along with the LLEV SNe II in our set. We note that the LLEV SNe II are systematically bluer than normal SNe II in all the phase range reported in the plot.[9] The latter could be due to low metallicity progenitors (where the lower the progenitor metallicity, the bluer the colour; Dessart et al. 2014), or a consequence of an ejecta–CSM interaction, which makes colours bluer than normal SNe II (e.g. Hillier & Dessart 2019) as in the case of SNe IIn/II, which are included in Fig. 4 for comparison.

The bottom part of Fig. 4 shows the evolution of the late-time $B - V$ colour of SN 1983K, compared with normal SNe II that we found in the literature with the *B*- and *V*-band photometry during 190–350 d since explosion, i.e. the phase range covered by the late-

[8]We remove SN 2009au from the D18 sample since it is in our LLEV SN II sample.

[9]In the case of SN 2009au, its $B - V$ colour curve was matched to the rest of LLEV SNe II in order to estimate $E^{\rm host}_{B-V}$ (see Section 2.3).

time $B - V$ colour of SN 1983K. This sample is listed in Table A13. We see that the $B - V$ colour evolution of SN 1983K is consistent with the rest of normal SNe II in the plot. We also include a set of SNe IIn (sample listed in Table A14) to depict the effect of a long-lasting ejecta–CSM interaction over the $B - V$ colours. We see that the ejecta–CSM interaction on SNe IIn makes their colour bluer than normal SNe II. The latter suggests that for SN 1983K, the late-time flux is dominated by the decay of ^{56}Co to ^{56}Fe.

4.4 Nickel mass

Assuming that the observed flux during the radioactive tail is due to the decay of ^{56}Co to ^{56}Fe, and that all the γ-rays from that decay are thermalized, the ^{56}Ni mass synthesized during an SN II explosion can be estimated as (e.g. Hamuy 2003)

$$\frac{M(^{56}\mathrm{Ni})}{\mathrm{M}_{\odot}} = \left(\frac{L_t}{L_*}\right) \exp\left[\frac{(t - t_0)/(1 + z) - 6.1\,\mathrm{d}}{111.26\,\mathrm{d}}\right], \quad (1)$$

where L_t is the bolometric luminosity measured at epoch t, $L_* = 1.271 \times 10^{43}$ erg s^{-1}, and t_0 and z are the explosion epoch and heliocentric redshift of the SN, respectively.

To estimate L_t for the LLEV SNe II in our set, we use

$$\log(L_t/L_*) = (\mu - V_{0,t} - \mathrm{BC})/2.5 - 7.38, \quad (2)$$

where $V_{0,t}$ is the V-band magnitude at epoch t during the radioactive tail corrected by extinction, μ is the SN distance modulus, and BC is the bolometric correction. For the latter, we assume the same BC for SNe II during the radioactive tail (BC $= 0.26 \pm 0.06$ mag; Hamuy 2001). For SN 2009aj, we convert the last Rr photometry (at 173 d since explosion) to V-band magnitude using $V - R$ and $V - r$ colours of normal SNe II nearly at the same epoch of the Rr photometry, obtaining $V = 20.60 \pm 0.13$ mag. For LSQ13fn, we compute $V = 26.24 \pm 0.30$ mag from its nebular spectrum (at 335 d since explosion). For SN 1983K, we measure a V-band radioactive tail slope (s_3) of 1.01 ± 0.02 mag $(100\,\mathrm{d})^{-1}$, which is consistent with the slope of 0.98 mag $(100\,\mathrm{d})^{-1}$ expected for the complete γ-ray trapping scenario. For SN 2008bm, SN 2009aj, and LSQ13fn, there are not enough photometric data during the nebular phase to estimate s_3. Since we cannot check the complete γ-ray trapping scenario for those SNe, we adopt their ^{56}Ni mass estimations as lower limits. ^{56}Ni mass values are listed in Table 1.

Fig. 5 shows the location of the LLEV SNe II (blue squares) in the log ^{56}Ni mass versus the absolute V-band magnitude at 50 d since explosion ($M_V^{50\mathrm{d}}$) space.[10] For comparison, we include normal SNe II (empty circles) in the A14 sample, which have ^{56}Ni mass values estimated in the same manner than our LLEV SNe II, and the normal SNe II in the Hamuy (2003) sample, where we recompute the ^{56}Ni masses using new estimations for the distance and host galaxy reddening (the SN set and parameters are listed in Table A15). We also include the SN IIn/II set (red diamonds). As noted by Hamuy (2003) and subsequently by other authors (e.g. Pejcha & Prieto 2015; Valenti et al. 2016; Müller et al. 2017), and as visible in Fig. 5, for normal SNe II there is a correlation between the ^{56}Ni mass and $M_V^{50\mathrm{d}}$. In order to characterize ,the distribution of normal SNe II, we fit a straight line (solid line), where the dashed lines indicate the $\pm 2\sigma$ limits. We note that SN 1983K is below the -2σ limit, i.e. at 50 d since explosion it is brighter than those explosions producing the same amount of ^{56}Ni. The latter, along with the colour evolution of SN 1983K (Fig. 4), indicates that for that SN there is a source of photons, still relevant at 50 d since explosion, which becomes negligible at the radioactive tail. We speculate that the source of these photons is the early interaction between the SN ejecta and the CSM.

[10]Since the errors in the log $(M(^{56}\mathrm{Ni}))$ versus $M_V^{50\mathrm{d}}$ space are dominated by errors in reddenings and/or distances, the confidence regions are elongated ellipsoids (e.g. Pejcha & Prieto 2015).

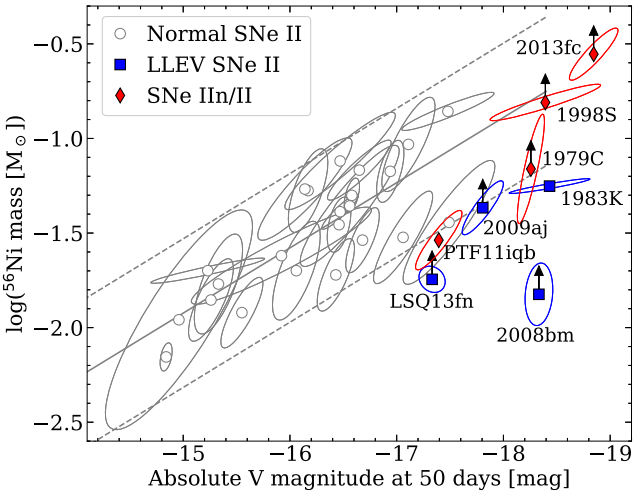

Figure 5. ^{56}Ni mass versus absolute V-band magnitude at 50 d since explosion, showing the normal SNe II (empty circles), the SNe IIn/II from the literature (red diamonds), and the LLEV SNe II in our set (blue squares). The ellipses indicate the 1σ statistical error. The solid line corresponds to a linear fit, where dashed lines indicate the 2σ error around the fit. Arrows indicate lower limits.

5 SPECTROSCOPIC PROPERTIES

In the previous section, we found evidence in favour of an early ejecta–CSM interaction scenario for LLEV SNe II. In this section, analysing the spectroscopic data, we present further evidence that reinforces this hypothesis.

5.1 Spectral evolution

Fig. 6(a) shows the early spectra of the LLEV SNe II (left-hand panel), along with zooms around Hδ, Hγ, and Hβ (middle panel) and Hα (right-hand panel). We can see that those SNe show broad Hα and Hβ in emission, centred in the laboratory wavelengths, and with no prominent absorption features. The latter is characteristic of an SN II ejecta interacting with a CSM, where the line broadening mechanism is dominated by electron scattering (Chugai 2001). The spectral feature located between Hγ and Hβ (prominent in SN 1983K and LSQ13fn, but weaker in SN 2009aj and SN 2009au spectra) corresponds to He II λ4686 possibly blended with N III $\lambda\lambda$4634-40-42 (Niemela et al. 1985) and C III λ4648 (Polshaw et al. 2016). The high temperature needed to produce the N III/C III/He II feature could come from the conversion of kinetic energy into thermal energy during an ejecta–CSM interaction, which favours this scenario.

Fig. 6(b) shows the spectra of SN 2009au and SN 2008bm at 23 and 74 d since explosion, respectively. Since the Hα profile in the SN 2008bm spectrum is highly contaminated by H II region lines (depicted as grey lines), we remove that contamination modelling the Hα profile as a mixture of three Gaussians (SN Hα absorption

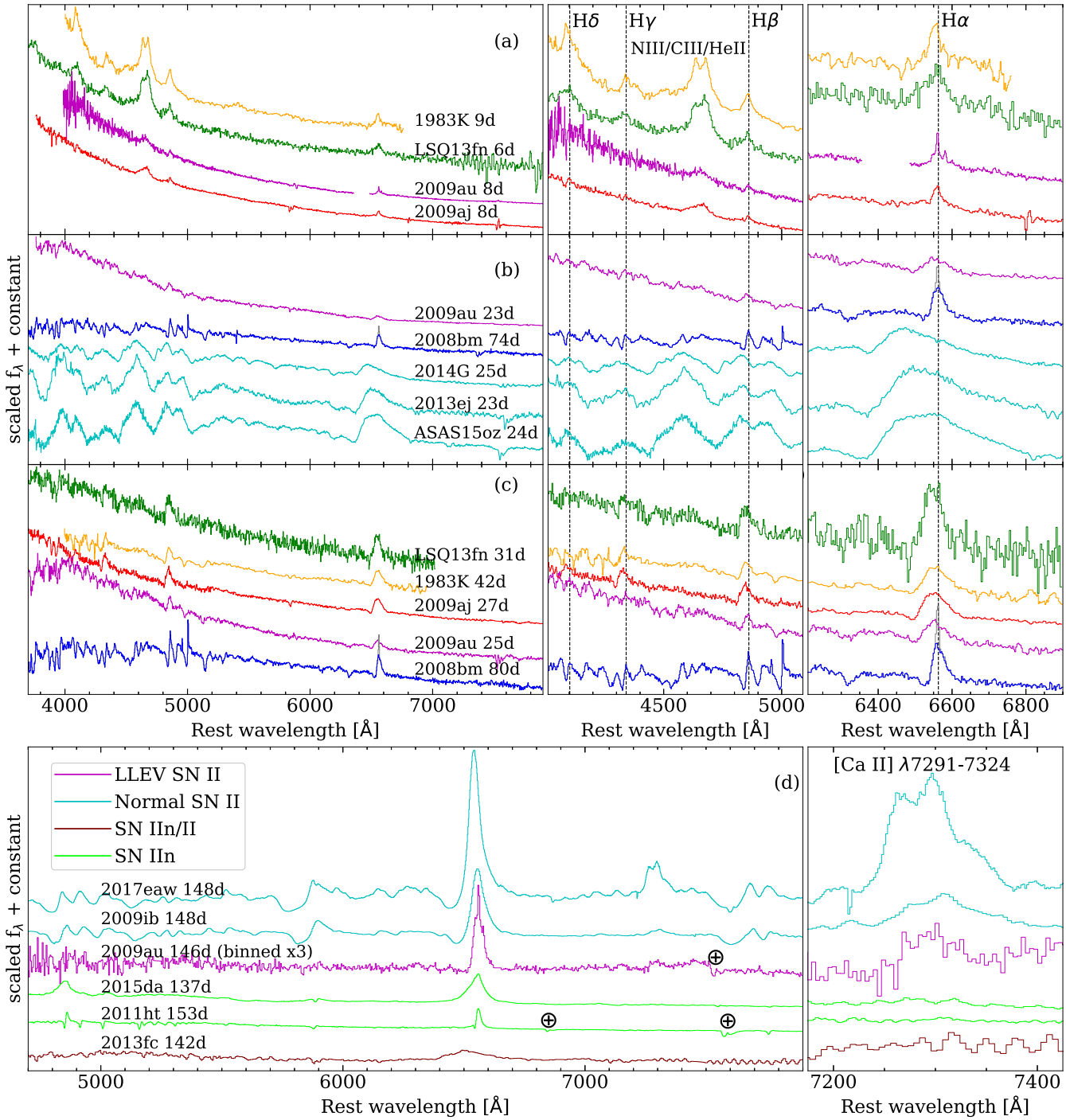

Figure 6. Panels (a)–(c) show the early spectra, the last spectra still affected by the ejecta–CSM interaction, and the first spectra showing Balmer absorptions for our LLEV SN II, respectively, and zooms around Hδ, Hγ, and Hβ (middle column) and Hα (right-hand column). In Panel (b), we also plot normal SNe II (cyan) for comparison. Panel (d): latest spectrum of SN 2009au compared with spectra of SNe IIn, SNe IIn/II, and normal SNe II at similar epochs, and a zoom around [Ca II] λ7291-7324 (right-hand panel). Circled crosses indicate the presence of telluric lines. Epochs are since the explosion. Spectra were corrected for redshift and reddening.

and emission, along with the Hα emission from the H II region). In the middle row of the right-hand column of Fig. 6, we see that the absorption part of the Hα P-Cygni profile is not strong. The latter could arise from the fact that SN 2008bm and SN 2009au are fast decliners, which typically have weaker Hα P-Cygni profile absorptions (e.g. Gutiérrez et al. 2017b), but also could indicate that the ejecta–CSM interaction is still ongoing. In Fig. 6(b), we also plot spectra of the fast decliners SN 2014G, SN 2013ej (e.g. Bose et al. 2015; Huang et al. 2015), and ASASSN-15oz (Bostroem et al. 2019) at epochs close in time to the SN 2009au spectrum. We see that the Hα P-Cygni absorption component of SN 2008bm and SN 2009au is weaker (and narrower) than those of the other fast

decliners, which indicates that the weakness of the Hα P-Cygni absorption component of SN 2008bm and SN 2009au is not only related to their high photometric decline rates but also due to still ongoing ejecta–CSM interaction.

Fig. 6(c) shows the spectra of LSQ13fn, SN 1983K, SN 2009aj, SN 2009au, and SN 2008bm at 31, 42, 27, 27, and 80 d since explosion, respectively. At these epochs, the LLEV SNe II in our set start to show the absorption part of the Hα P-Cygni profile, and the emission peaks appear blueshifted, where the broader the emission the more blueshifted the peak. The latter characteristic is common in normal SNe II (Anderson et al. 2014a), indicating that the effect of the ejecta–CSM interaction decreases substantially after 4–11 weeks since explosion.

Fig. 6(d) shows the latest spectrum of SN 2009au at 146 d since explosion, compared to spectra at similar epochs of SNe IIn (green) and SNe IIn/II (brown) that we found in the literature, and some normal SNe II (cyan). The most prominent spectral feature in the SN 2009au spectrum is the Hα profile in emission, while the rest of the spectrum seems featureless compared to normal SNe II, as in the case of the SNe IIn and SNe IIn/II in the plot. However, we detect [Ca II] λ7291-7324 that is present in normal SNe II but absent in the SN IIn and SN IIn/II spectra in the plot.

The left-hand side of Fig. 7 shows the near-IR spectra of SN 2009aj combined with the closest (in time) optical spectra, along with zooms around Hα (middle column), Pβ and the spectral feature corresponding to Pγ blended with He I λ10830 and Sr II λ10920 (right-hand column). For comparison, we also include combined optical and near-IR spectra of the SNe IIn (red) 2015da (Tartaglia et al. 2020) and 2010jl (Zhang et al. 2012; Borish et al. 2015), the SNe IIn/II (green) 1998S, 2007pk, and 2013fc, and the normal SN II 2017eaw (e.g. Szalai et al. 2019). All the previous SNe II were found having optical and near-IR spectra close in time to the combined spectra of SN 2009aj. At 1–2 weeks since explosion, the spectrum of SN 2009aj does not show the Pβ profile, being more similar to the spectrum of SN IIn 1998S than to the normal SN II 2017eaw. The absorption at 1.27 μm in the SN 2009aj spectrum is not followed by a redder emission, so this feature might not belong to the SN. At 3–4 weeks since explosion, the spectrum of SN 2009aj is more similar to the normal SN II 2017eaw than to the SN IIn 2015da, but with Hα, Pβ, and Pγ/He I/Sr II profiles weaker and narrower than the observed in SN 2017eaw. At 9–10 weeks since explosion, the Hα profile and the Pβ emission component are more similar to SNe IIn/II and SN 2017eaw, but still weaker.

The aforementioned characteristics of the near-IR spectral evolution of SN 2009aj are quite similar to those found in the optical spectral evolution of the LLEV SNe II.

5.2 Weakness of metal lines

The top part of Fig. 8 shows the evolution of the Fe II λ5018 pEW of the LLEV SNe II in our set (coloured symbols), compared to the normal SNe II in the G17 sample (empty circles). We see that the LLEV SNe II are mostly below the -1σ limit (dashed line) of the G17 sample, which indicates the weakness of metal lines in the LLEV SNe II spectra in all the phase range reported in the plot.

Polshaw et al. (2016) had already reported the weakness of metal lines in the spectra of LSQ13fn compared to normal SNe II. In that work, one of the parameters that they suggested to explain the weakness of metal lines is a low metallicity of the SN progenitor. In fact, Dessart et al. (2014) explored theoretically the dependence on the SN II progenitor metallicity of some spectral features. The general behaviour they obtained is the lower the progenitor metallicity, the weaker the metal lines. A lower metallicity also implies a lower line blanketing and therefore a colour bluer than other SNe II with a higher metallicity, which, in principle, could explain the blue colour we observe in LLEV SNe II.

Nevertheless, the strength of metal lines not only depends on the progenitor metallicity, but also on the temperature of the line formation region (which modifies the opacity) and, when the SN is surrounded by a CSM, on the contribution to the flux generated from the ejecta–CSM interaction (Leloudas et al. 2015). Regarding the temperature, Anderson et al. (2016, hereafter A16) show that the pEW of the Fe II λ5018 line in normal SN II spectra increases with the $V-I$ and $V-i$ colour, which are used as a proxy for temperature.

The bottom part of Fig. 8 shows the Fe II λ5018 pEW, as a function of the $B-V$ colour. In the plot, we see that LLEV SNe II occupy a region similar to SNe IIn/II with both groups scattering around the $+1\sigma$ limit of normal SNe II. This indicates that in LLEV SNe II the weakness of metal lines is at least partially due to the higher temperature in the line-forming region, but also that the line dilution plays a role. Regarding the latter, to quantify its effect to first order, we select SN 2008M (A14, G17) because it is one of the bluest normal SNe II in the D18 sample. With this, we can isolate as best as possible the effect of CSM dilution on the pEW of the metal lines from the similar effect of temperature, we have analysed previously. Fig. 9 shows the spectrum of SN 2009aj at 39 d since explosion (red line) and a spectrum of SN 2008M nearly at the same epoch and scaled to the SN 2009aj distance (grey line). Spectra of SN 2009aj and SN 2008M have Fe II λ5018 pEW of 7.1 and 9.7 Å, respectively. In order to include the contribution of a CSM to the flux of SN 2008M, we model the CSM as a blackbody. We choose the CSM parameters such that the continuum of SN 2008M plus the CSM matches to the continuum of SN 2009aj, which is reached using a radius of 10^{15} cm and a temperature of 7200 K. The Fe II λ5018 pEW of the composite spectrum is of 5.7 Å, which matches better to the value for SN 2009aj. Therefore, even when the SN 2008M spectrum is not as blue as the spectrum of SN 2009aj, and the oxygen abundance at the site of SN 2008M (8.43 dex; A16, which we use as a proxy for the progenitor metallicity) is higher than the value for SN 2009aj (8.29 dex; see Table 1), the flux contribution due to the ejecta–CSM interaction seems to be an efficient driver of the observed weakness of metal lines in its spectra.

Fig. 10 shows the Fe II λ5018 pEW at 50 d since explosion, as a function of the $B-V$ colour (corrected for $E^{\rm host}_{B-V}$) at the same epoch (left-hand side), and as a function of the oxygen abundance in the N2 calibration of Marino et al. (2013) (right-hand side) for the LLEV SNe II in our set (coloured filled symbols). For comparison, we plot the normal SNe II in the A16 sample[11] (grey empty circles, where we use the colour curves plotted in Fig. 4 to compute $B-V$ colours at 50 d since explosion), and the SNe IIn/II (green empty symbols). In the left-hand panel, we see that SN 1998S, SN 2009aj, and LSQ13fn have similar Fe II λ5018 pEW values and $B-V$ colours, while in the right-hand panel, we see that the same SNe have different oxygen abundances. The latter indicates that (1) the metallicity is not a dominant component determining the Fe II λ5018 pEW values as $B-V$ colour is, or (2) SN 1998S and LSQ13fn suffer

[11] We remove SN 2008bm, SN 2009aj, and SN 2009au from the sample since they are in our LLEV SN II sample.

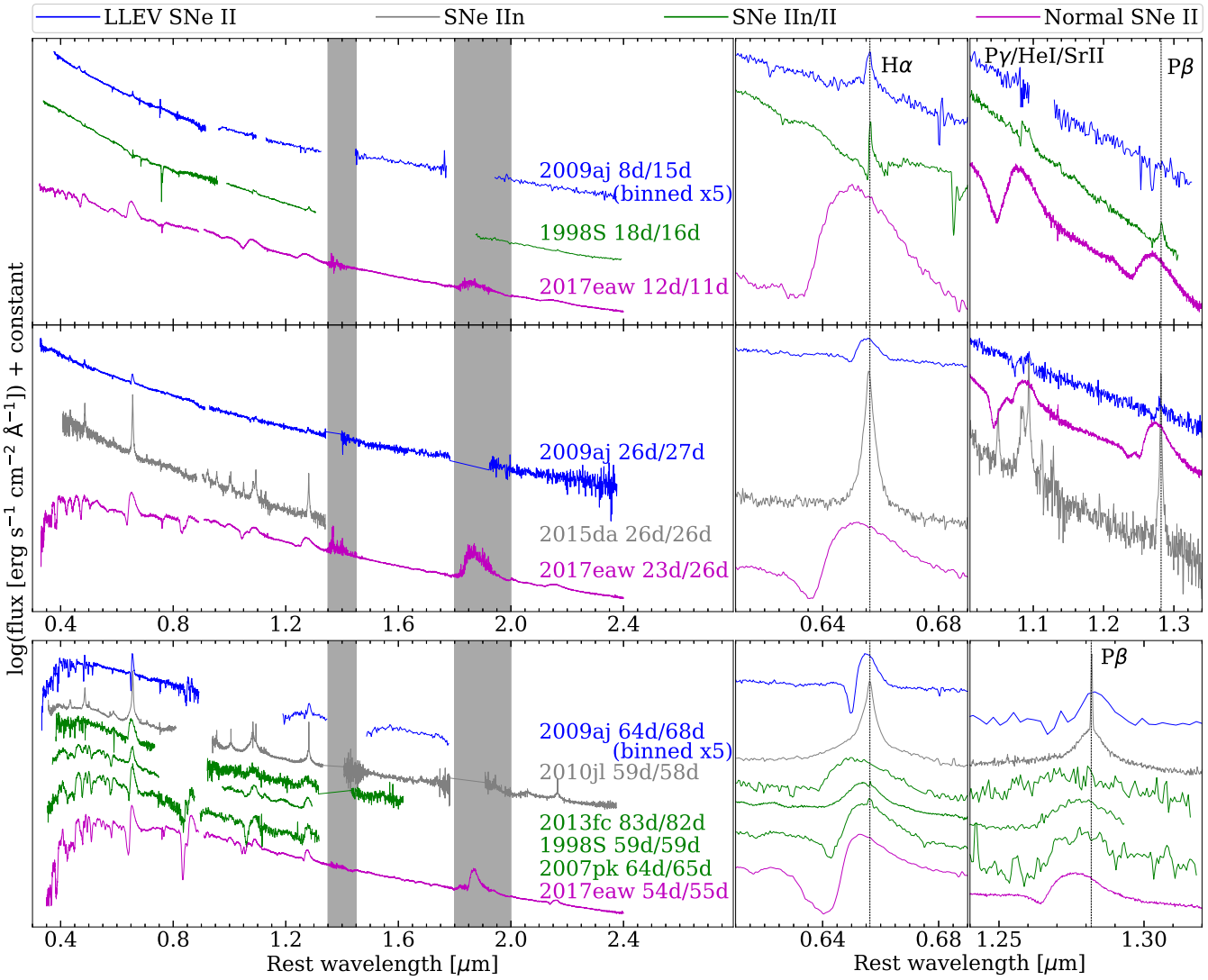

Figure 7. Left-hand column: near-IR spectra of SN 2009aj combined with the closest in time optical spectra (blue), compared with the combined optical and near-IR spectra of SNe IIn (grey), SNe IIn/II (green), and normal SN II 2017eaw (magenta) at similar epochs. Middle column: zooms around Hα. Right-hand column: zooms around the Pγ/He I/Sr II and Pβ profiles.

more line dilution compared to SN 2009aj. In Fig. 10, we also see SN 2013fc, LSQ13fn, and SN 1983K having similar $B-V$ colour and oxygen abundances, but different Fe II λ5018 pEW values. One explanation for this difference is that SN 1983K and LSQ13fn suffer more line dilution than SN 2013fc. Based on these findings, we suggest that the progenitor metallicity is not the main driver of the weakness of metal lines seen on LLEV SNe II spectra, but a combination of higher temperatures at the line formation region and line dilution (both being consequence of an early ejecta–CSM interaction).

5.3 Expansion velocities

Fig. 11 shows the evolution of the expansion velocities, measured through the Fe II λ5169 minimum absorption lines ($v_{\rm FeII}$), of the LLEV SNe II in our set (coloured symbols) and the normal SNe II in the G17 sample 11 (empty circles). Expansion velocities for LLEV SNe II are all below the -1σ limit (dashed line) of the G17 sample (2820 km s^{-1} at 50 d since explosion). In particular, SN 2008bm and SN 2009au have expansion velocities similar to SN 1999br (orange-dashed line), which is one of the SNe II with the lowest expansion velocities in the G17 sample ($v_{\rm FeII} \approx 1550$ km s^{-1} at 50 d since explosion). These low expansion velocities can be explained by the loss of kinetic energy by the ejecta due to their interaction with CSM.

6 DISCUSSION

6.1 A break in the magnitude–velocity relation

As we have seen in Section 4.1 and 5.3, LLEV SNe II are characterized by having luminous peak magnitudes and low expansion velocities. This is not expected in a scenario where more energetic SN II explosions that produce high luminosities also have high expansion velocities. This trend is shown in Fig. 12, where we plot the V-band absolute magnitude and the expansion velocity, both at 50 d post-explosion, for the normal SNe II in the A14 SN sample (grey circles, where expansion velocities are from table 3 of

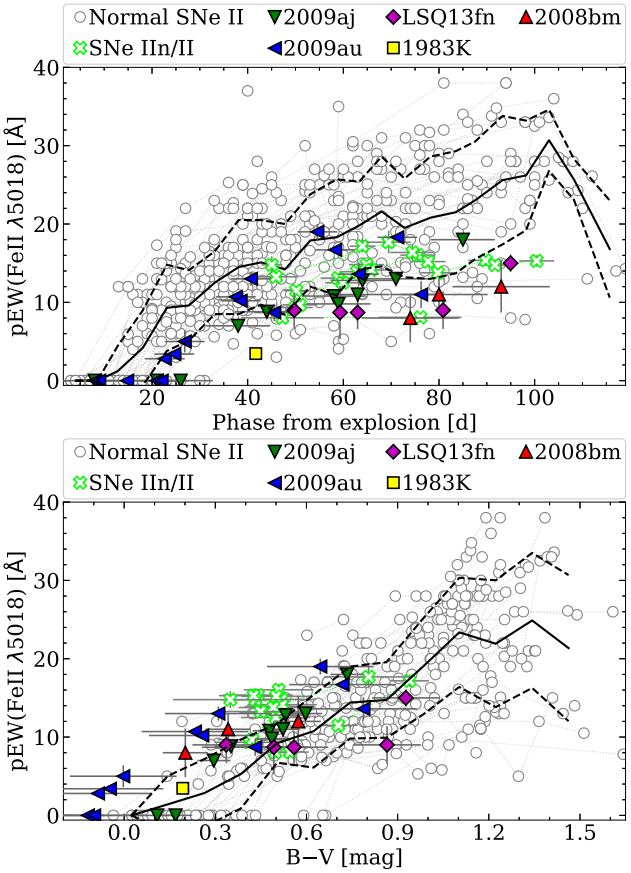

Figure 8. Evolution of the Fe II λ5018 pEW, as a function of the time since explosion (top panel) and the $B - V$ colour (bottom panel), of the LLEV SNe II (filled symbols), the SNe IIn/II from the literature (empty crosses), and the normal SNe II in the G17 sample (empty circles). Black solid and dashed lines correspond to the mean values and standard deviations, respectively.

Gutiérrez et al. 2017b). To characterize the distribution of the A14 sample in this space, we perform a Gaussian process fit (solid line), where dashed lines indicate the $\pm 3\sigma$ error around the fit. We can see that the LLEV SNe II[12] (blue squares) populate a region where the only known member was LSQ13fn, marking a discrepancy of 2–3 mag with respect to the trend obtained with the A14 sample. At this point, it is not clear whether the LLEV SNe II can be considered as a separated class of SNe II, or whether they are part of a continuum in the SN II distribution induced by an increasing ejecta–CSM interaction.

To test the latter, we include in Fig. 12 the SNe IIn/II set. We see that SN 1998S, SN 2008fq, SN 2013fc, and, possibly, SN 1979C, are brighter than the 3σ limit. However, they do not fill the gap between the distribution of normal SNe II and the LLEV SNe II.

Fig. 13 shows the absolute magnitude as a function of the expansion velocity and the $B - V$ colour, all at 50 d since explosion of the LLEV SNe II in our set (blue squares). In this space, we see that the LLEV SNe II seem to form a separated set of objects from the rest of normal SNe II (grey circles). With the aim to confirm this visual finding, we run the mean-shift algorithm to search for

[12]For SN 1983K and SN 2008bm, we extrapolate the expansion velocities at 50 d since explosion using the power law given in Nugent et al. (2006).

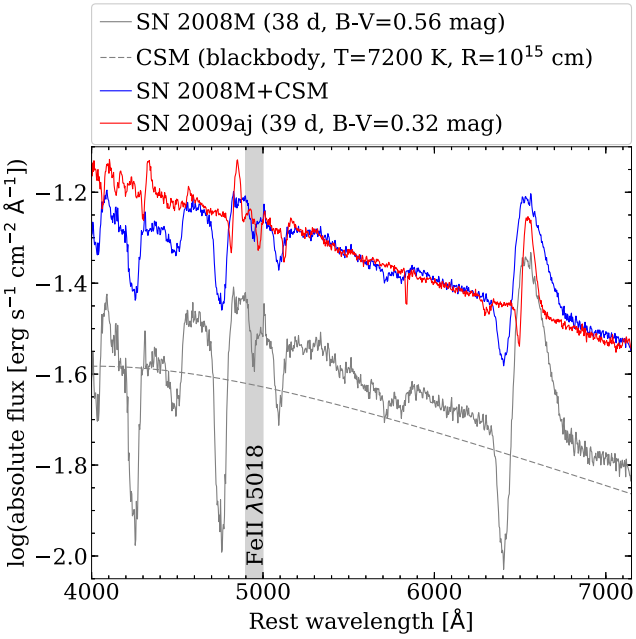

Figure 9. Comparison of the spectrum of SN 2009aj at 39 d since explosion (red line) with a composite spectrum (blue line), which is the sum of the SN 2008M spectrum at 38 d since explosion (grey line) and a blackbody continuum (dashed line). Gray region indicates the location of the Fe II λ5018 line.

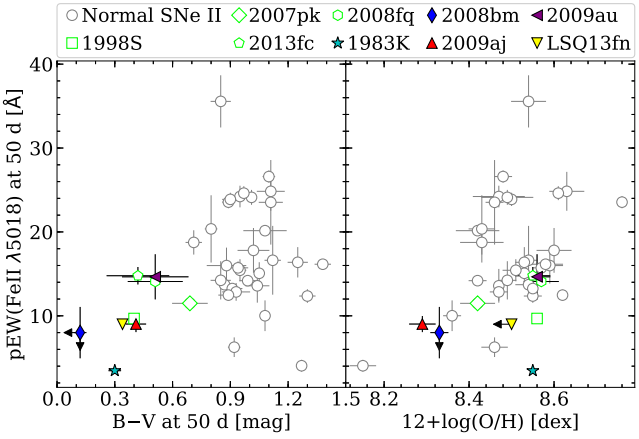

Figure 10. pEW of the Fe II λ5018 line at 50 d since explosion as a function of the $B - V$ colour (corrected for reddening) at the same epoch (left-hand side), and as a function of the oxygen abundance (right-hand side), showing the LLEV SNe II in our set (coloured filled symbols), the SNe IIn/II from the literature (green empty symbols) and the normal SNe II in the A16 sample (grey empty circles). Arrows indicate upper limits.

clusters in this space. We perform simulations where points are moved within their errors (assuming a normal distribution), and we find that in all of the realizations the LLEV SNe II form a separated group with respect to the rest of SNe II. Although given the low number of LLEV SNe II, this result has to be taken with caution, the fact that these SNe always cluster in a different parameter space region, indicates that these SNe could indeed be a new sub-type of SNe II.

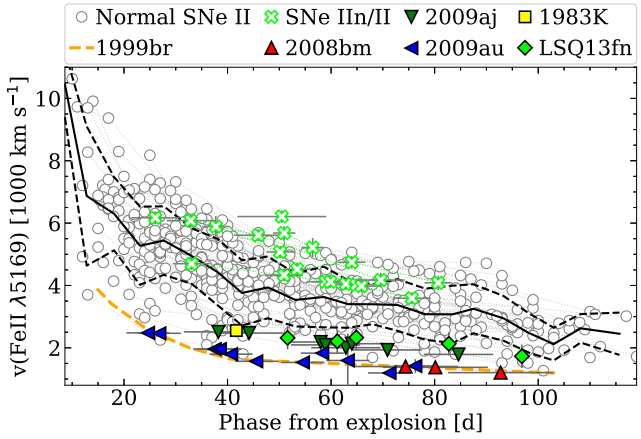

Figure 11. Evolution of the expansion velocities, measured through the Fe II λ5169 minimum absorption lines, of the LLEV SNe II (filled symbols), the SNe IIn/II from the literature (empty crosses), and the normal SNe II in the G17 sample (empty circles). Black solid and dashed lines correspond to the mean values and standard deviations, respectively, of the expansion velocities in the G17 sample. The orange-dashed line corresponds to the expansion velocities for SN 1999br.

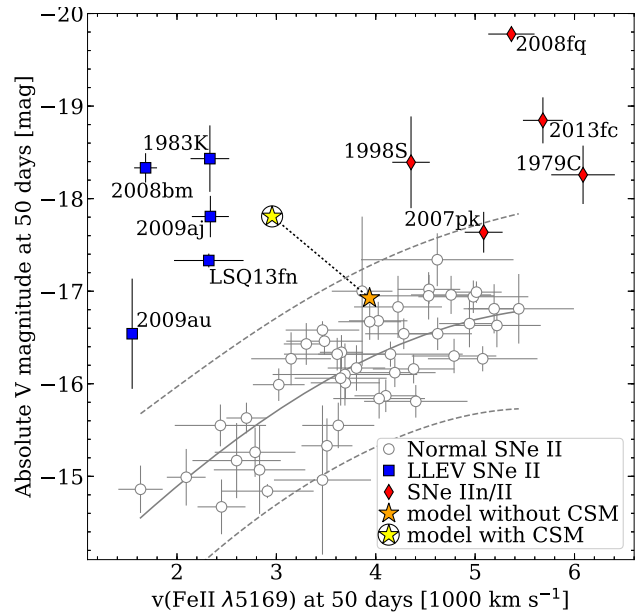

Figure 12. Absolute *V*-band magnitude versus expansion velocity, both at 50 d since explosion, showing the LLEV SN II set (blue squares), the normal SNe II in the A14 sample (empty circles), and the SNe IIn/II from the literature (red diamonds). The solid line corresponds to the Gaussian process fit, where dashed lines indicate the 3σ error around the fit. We also plot the location of our model for SN 2009aj (see Section 6.2) without (orange star) and with (circled yellow star) CSM.

6.2 Interaction of the ejecta with a massive CSM

As mentioned in the previous paragraphs, a scenario where the ejecta of a normal SN II interacts with a CSM medium could explain all the characteristics observed in LLEV SNe II. In fact, during the ejecta–CSM interaction, part of the kinetic energy is converted into thermal energy and photons, which slows down the ejecta, increases the temperature and luminosity, and veils the spectral lines.

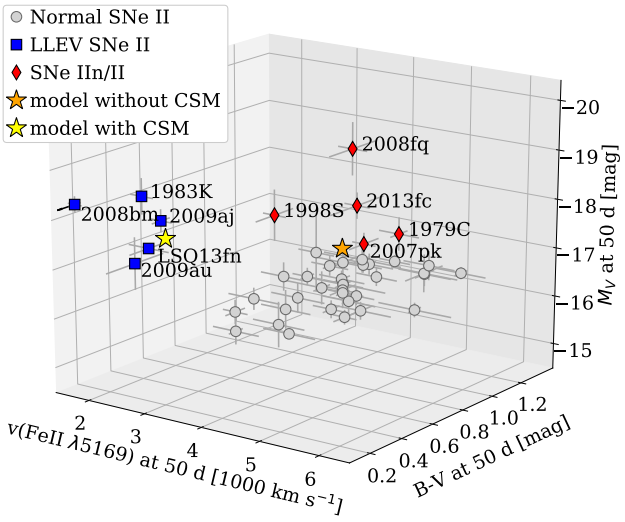

Figure 13. Absolute *V*-band magnitude versus expansion velocity and $B - V$ colour, all at 50 d since explosion, for the LLEV SNe II in our set (blue squares), the normal SNe II in the A14/D18 sample (grey circles), and the SNe IIn/II from the literature (red diamonds). The $B - V$ colour of SN 2008bm is an upper limit. We also plot the location of our model for SN 2009aj (see Section 6.2) without (orange star) and with (yellow star) CSM.

In order to test whether the ejecta–CSM interaction is responsible of converting a normal SN II into a LLEV SN II, we perform hydrodynamical simulations. We focus on the modelling of SN 2009aj here because its explosion epoch and host galaxy colour excess are better constrained than those for SN 2008bm and SN 2009au. We adopt the same numerical method as in Moriya et al. (2017, 2018) and use the radiation hydrodynamics code STELLA (Blinnikov et al. 1998, 2000, 2006) for our numerical light curve modelling.

We take the 14 $M_\odot$ progenitor model in Moriya et al. (2018) and attached a dense CSM above the progenitor by adopting the β law wind velocity. We take one model with the mass-loss rate of 3×10^{-2} $M_\odot$ yr^{-1}, the terminal wind velocity of 10 km s^{-1}, $\beta = 5$, and the dense CSM radius of 10^{15} cm. This dense CSM has a mass of 3.6 $M_\odot$. When we explode the progenitor in this system with the explosion energy of 8×10^{50} erg, we obtain the *UBVRI* absolute light curves, and expansion velocities as in Fig. 14 (solid lines). We can see that the observed absolute magnitudes and expansion velocities of SN 2009aj (empty symbols) match well to the numerical results, adopting an explosion epoch 1.5 d prior to the last non-detection.[13]

The effect on the luminosity–velocity relation produced by the interaction of the ejecta with a massive CSM is depicted in Fig. 12. We can see that the SN II model without CSM (orange star), consistent with the rest of the observed SNe II, is translated outside of the 3σ limit in direction to the location of the LLEV SNe II if we include a massive CSM (circled yellow star).

6.3 The observed fraction of LLEV SNe II

In order to estimate a first approximation of the fraction of LLEV within the normal SN II family, we use the monitoring campaign carried out by the CHASE survey. Since LLEV SNe II are typically

[13]Given the limiting magnitude of the last non-detection, we cannot discard the presence of the SN at >18.4 mag.

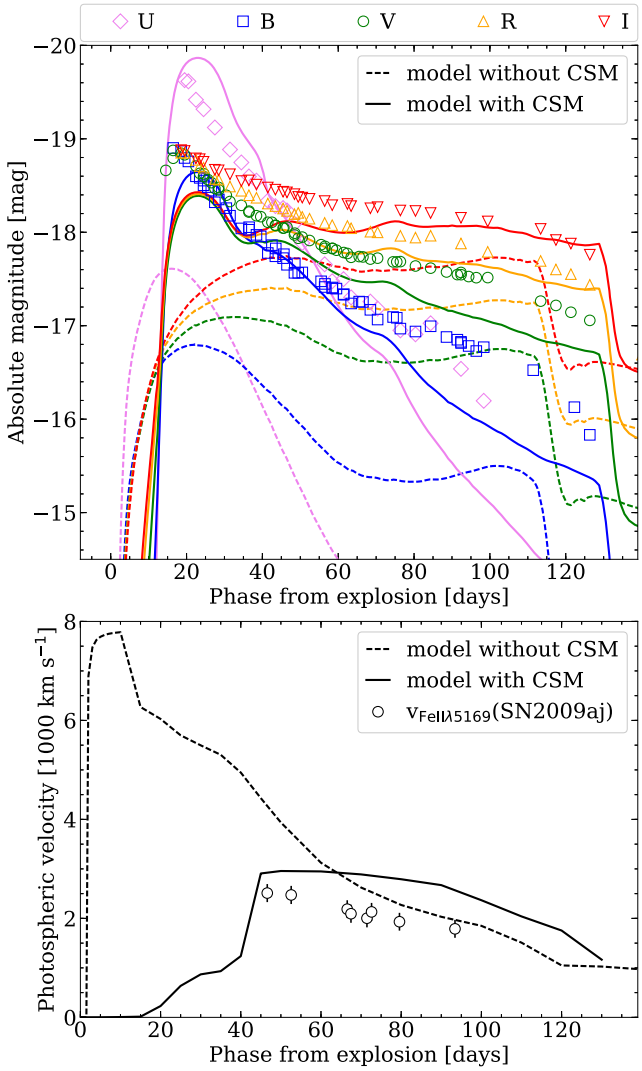

Figure 14. Absolute *UBVRI* light curves (top panel) and expansion velocities (middle panel) of our model with CSM (solid lines) and of SN 2009aj (empty symbols). The same model but without CSM (dashed lines) is displayed for comparison.

more luminous than normal SNe II, and given that the CHASE is a magnitude-limit survey, the estimation of the fraction of LLEV SNe II we will provided should be regarded as an upper limit.

During 2008 March–2014 December, CHASE reported the discovery of 46 normal SNe II and 3 SNe IIn (among them, SN 2009aj and SN 2009au). In addition, we include 58 normal SNe II and 6 SNe IIn discovered by other surveys during the same period, which were discovered by CHASE independently. In order to identify possible LLEV SNe II in the CHASE normal SN II sample, we check the classification reports (and classification spectra, if they are available). We select as possible LLEV SNe II those SNe whose classification spectra best match to a subluminous SN II (e.g. SN 2005cs), or have low expansion velocities (e.g. Hα $\lesssim$ 5000 km s^{-1}). From this list, we discard those SNe having absolute magnitude[14] (at the moment of the discovery or in posterior confirmation epochs) consistent with subluminous SNe II ($\gtrsim -16.0$ mag; Lisakov et al. 2018). From the CHASE SN IIn sample, we select as possible LLEV SN II those SNe IIn that spectroscopically do not evolve as an SN IIn but as a normal SN II with narrow P-Cygni profiles. For this, we use the information available in the literature.

Among the 104 normal SNe II, 15 show spectral characteristics consistent with low expansion velocities, of which 7 are published subluminous SNe II, and 6 have absolute magnitudes (corrected for $E^{\rm host}_{B-V}$ inferred from Na I D at the redshift of the host galaxy) >-15.5 mag. Only SN 2009aj shows narrow P-Cygni profiles and high luminosities, while for SN 2010jc we do not have enough information to confirm or discard it. Among the nine SNe IIn, seven of them evolve as SNe IIn. Only SN 2009au shows a posterior evolution different than an SN IIn, while for SN 2008gm there is not enough information to confirm or discard its LLEV nature. If we consider SN 2009aj and SN 2009au as the only LLEV SNe II in the CHASE sample, then its fraction could be around 2 per cent. On the other hand, if we consider all the unconfirmed candidates (SN 2010jc and SN 2008gm) as LLEV SNe II, then the upper limit increases to 4 per cent. The low fraction of LLEV SNe II points towards an uncommon progenitor, which should have experienced a high mass-loss rate close in time to core collapse in order to generate a sufficiently massive shell ($\sim$4 M$_\odot$) close to its surface to produce the spectroscopic and photometric characteristics that we observe in LLEV SNe II.

6.4 Impact on SNe II as distance indicators

Since the LLEV SNe II do not follow the luminosity–velocity relation observed for normal SNe II, we have to analyse their impact over the use of normal SNe II as distance indicators.

As mentioned in Rodríguez et al. (2019), the SN II distance precision using the photospheric magnitude method (Rodríguez, Clocchiatti & Hamuy 2014) could be up to 0.23 mag within a 99 per cent of confidence level. In this case, the location of the LLEV SNe II ($\geq$2 mag brighter than the expected from their expansion velocities) in the *Hubble* diagram will be $\geq 8.7\sigma$ below the Hubble law fit. Therefore, these events can be easily discarded with a sufficient amount of data.

Since the oxygen abundance of LLEV SNe II is not necessarily low, we do not have evidence that those SNe are related to low metallicity galaxies, so we do not expect that the fraction of LLEV SNe II will increase with redshift (e.g. $z > 0.5$) as consequence of the evolution of the metallicity of the Universe. However, we expect to find a higher fraction of LLEV SNe II due to the Malmquist bias. For example, for the Rubin Observatory Legacy Survey of Space and Time (LSST) the *r*-band 5σ limiting magnitude is estimated to be $\sim$24.3 mag, so for $z \geq 0.5$ we expect to detect SNe II with $M_r \lesssim -18.0$ mag. In this case, the observed fraction of LLEV SNe II could be as high as 10–18 per cent, so the LLEV SNe II will be only $\geq$2.9–3.9σ below the Hubble law, which makes it difficult to recognize them as outliers. This means that the existence of LLEV SNe II has to be taken into account if normal SNe II at high redshifts are used to derive cosmological parameters. Nevertheless, as shown in this work, the current sample has expansion velocities, which are in the lower end of the normal SN II distribution, therefore a cut on expansion velocities could greatly reduce their contamination.

7 CONCLUSIONS

In this work, we presented optical and near-IR data of SN 2008bm, SN 2009aj, and SN 2009au. From the analysis of these data together with already published data, we found that they show similar characteristics with those of SN 1983K and LSQ13fn. In the luminosity–expansion velocity plane this possible family of

[14]Discovery and confirmation magnitudes reported by CHASE are obtained from unfiltered images, which are similar to *R*-band magnitudes.

SNe II, that we call LLEV, forms a separate group which have *V*-band absolute magnitudes 2–3 mag brighter that those expected from their expansion velocities by the luminosity–velocity relation observed for normal SNe II.

The ejecta–CSM interaction observed in LLEV SNe II lasts up to 4–11 weeks since the explosion. Subsequently, spectra show P-Cygni profiles characterized by low expansion velocities, and weakness of metal lines. We found evidence that the metal line weakness seems not to be related to the metallicity of the progenitor but with a combined effect of the line dilution due to the contribution of the CSM to the flux, and the higher temperatures than normal SNe II at similar epochs. Through hydrodynamic simulations, which consider an RSG progenitor of 14 $M_{\odot}$ with an explosion energy of 8×10^{50} erg, we found that the high-luminosity and low expansion velocities seen on SN 2009aj can be explained if the ejecta interacts with a CSM of $\sim$3.6 $M_{\odot}$ located very close to the progenitor.

Based on the discoveries by the CHASE survey, we estimated an upper limit for the LLEV SNe II fraction to be 2–4 per cent of all normal SNe II. This low fraction, together with the high CSM mass, we obtained from the hydrodynamic simulations, may indicate an uncommon progenitor with a high mass-loss rate close in time to core collapse in order to generate a sufficiently massive shell close to its surface. Based on the available data, it is unclear whether the LLEV SNe II are a separated class of SNe II with a different progenitor system, or there is a continuum of objects connecting them with the normal SNe II. It is necessary to populate the luminosity–velocity space with more LLEV SNe II in order to reveal the nature of these peculiar SNe II. Finally, we showed that, based on the current sample, LLEV SNe II should not represent a severe contaminant in the use of normal SNe II as standardizable candles.

ACKNOWLEDGEMENTS

We gratefully acknowledge the support of the CSP-I by NSF under grants AST-0306969, AST-0607438, and AST-1008343. OR, GP, AC, FF, and JLP acknowledge support by the Ministry of Economy, Development, and Tourism's Millennium Science Initiative through grant IC120009, awarded to The Millennium Institute of Astrophysics, MAS. OR acknowledge support from CONICYT PAI/INDUSTRIA 79090016. TJM is supported by the Grants-in-Aid for Scientific Research of the Japan Society for the Promotion of Science (JP17H02864, JP18K13585) and by Japan Society for the Promotion of Science Open Partnership Bilateral Joint Research Project between Japan and Chile. Support for JLP is provided in part by FONDECYT through the grant 1191038. CPG acknowledges support from EU/FP7-ERC grant no. [615929]. MDS is funded by a project grant (8021-00170B) from the Independent Research Fund Denmark and a generous grant (13261) from VILLUM FONDEN. Numerical computations were in part carried out on PC cluster at Center for Computational Astrophysics, National Astronomical Observatory of Japan. NBS acknowledges support from the NSF through grant AST-1613455, and through the Texas A&M University Mitchell/Heep/Munnerlyn Chair in Observational Astronomy. Additional support has been provided by the George P. and Cynthia Woods Mitchell Institute for Fundamental Physics and Astronomy. This work is partially based on observations collected at the European Southern Observatory under ESO programmes 082.A-0526 and 083.D-0970. This paper is based on observations obtained at the Gemini Observatory, Cerro Pachon, Chile (Gemini Program GS-2009A-Q-43). This research has made use of the NASA/IPAC Extragalactic Database (NED), which is operated by the Jet Propulsion Laboratory, California Institute of Technology, under contract with the National Aeronautics and Space Administration.

REFERENCES

Anderson J. P. et al., 2014a, MNRAS, 441, 671
Anderson J. P. et al., 2014b, ApJ, 786, 67 (A14)
Anderson J. P. et al., 2016, A&A, 589, A110 (A16)
Andrews J. E. et al., 2011, ApJ, 731, 47
Balinskaia I. S., Bychkov K. V., Neizvestnyi S. I., 1980, A&A, 85, L19
Baltay C. et al., 2013, PASP, 125, 683
Barbon R., Ciatti F., Rosino L., Ortolani S., Rafanelli P., 1982, A&A, 116, 43
Benetti S. et al., 2016, MNRAS, 456, 3296
Blinnikov S. I., Eastman R., Bartunov O. S., Popolitov V. A., Woosley S. E., 1998, ApJ, 496, 454
Blinnikov S., Lundqvist P., Bartunov O., Nomoto K., Iwamoto K., 2000, ApJ, 532, 1132
Blinnikov S. I., Röpke F. K., Sorokina E. I., Gieseler M., Reinecke M., Travaglio C., Hillebrand t W., Stritzinger M., 2006, A&A, 453, 229
Borish H. J., Huang C., Chevalier R. A., Breslauer B. M., Kingery A. M., Privon G. C., 2015, ApJ, 801, 7
Bose S. et al., 2013, MNRAS, 433, 1871
Bose S. et al., 2015, ApJ, 806, 160
Bose S., Kumar B., Misra K., Matsumoto K., Kumar B., Singh M., Fukushima D., Kawabata M., 2016, MNRAS, 455, 2712
Bostroem K. A. et al., 2019, MNRAS, 562
Branch D., Falk S. W., McCall M. L., Rybski P., Uomoto A. K., Wills B. J., 1981, ApJ, 244, 780
Chandra P., Soderberg A., 2008, Astron. Telegram, 1869, 1
Chandra P., Soderberg A., 2009, Astron. Telegram, 2351, 1
Chandra P., Chevalier R. A., Chugai N., Fransson C., Soderberg A. M., 2015, ApJ, 810, 32
Chugai N. N., 2001, MNRAS, 326, 1448
Ciatti F., Rosino L., Bertola F., 1971, Mem. Soc. Astron. Italiana, 42, 163
Clocchiatti A. et al., 1996, AJ, 111, 1286
Contreras C. et al., 2010, AJ, 139, 519
Crook A. C., Huchra J. P., Martimbeau N., Masters K. L., Jarrett T., Macri L. M., 2007, ApJ, 655, 790
Dall'Ora M. et al., 2014, ApJ, 787, 139
Das S., Ray A., 2017, ApJ, 851, 138
de Jaeger T. et al., 2018, MNRAS, 476, 4592 (D18)
de Vaucouleurs G., de Vaucouleurs A., Buta R., Ables H. D., Hewitt A. V., 1981, PASP, 93, 36
Dessart L. et al., 2008, ApJ, 675, 644
Dessart L. et al., 2014, MNRAS, 440, 1856
Drake A. J., Djorgovski S. G., Williams R., Mahabal A., Graham M. J., Beshore E. C., Larson S. M., Christensen E., 2008, Astron. Telegram, 1447, 1
Drake A. J. et al., 2009, ApJ, 696, 870
Elias-Rosa N. et al., 2016, MNRAS, 463, 3894
Elmhamdi A. et al., 2003, MNRAS, 338, 939
Faran T. et al., 2014, MNRAS, 445, 554
Fassia A. et al., 2000, MNRAS, 318, 1093
Fassia A. et al., 2001, MNRAS, 325, 907
Filippenko A. V., 1988, AJ, 96, 1941
Fitzpatrick E. L., 1999, PASP, 111, 63
Fixsen D. J., Cheng E. S., Gales J. M., Mather J. C., Shafer R. A., Wright E. L., 1996, ApJ, 473, 576
Förster F. et al., 2018, Nat. Astron, 2, 208
Fransson C. et al., 2014, ApJ, 797, 118
Galbany L. et al., 2016, AJ, 151, 33
Gutiérrez C. P. et al., 2017a, ApJ, 850, 89 (G17)
Gutiérrez C. P. et al., 2017b, ApJ, 850, 90
Hamuy M. A., 2001, PhD thesis, The University of Arizona
Hamuy M., 2003, ApJ, 582, 905
Hamuy M., Pinto P. A., 2002, ApJ, 566, L63

Hamuy M., Suntzeff N. B., Gonzalez R., Martin G., 1988, AJ, 95, 63
Hamuy M. et al., 2001, ApJ, 558, 615
Hamuy M. et al., 2006, PASP, 118, 2
Hicken M. et al., 2017, ApJS, 233, 6
Hillier D. J., Dessart L., 2019, A&A, 631, A8
Ho W. C. G., Van Dyk S. D., Peng C. Y., Filippenko A. V., Leonard D. C., Matheson T., Treffers R. R., Richmond M. W., 2001, PASP, 113, 1349
Huang F. et al., 2015, ApJ, 807, 59
Huang F. et al., 2016, ApJ, 832, 139
Humphreys R. M., Davidson K., Jones T. J., Pogge R. W., Grammer S. H., Prieto J. L., Pritchard T. A., 2012, ApJ, 760, 93
Inserra C. et al., 2012, MNRAS, 422, 1122
Inserra C. et al., 2013, A&A, 555, A142
Jang I. S., Lee M. G., 2017, ApJ, 836, 74
Kangas T. et al., 2016, MNRAS, 456, 323
Khazov D. et al., 2016, ApJ, 818, 3
Krisciunas K. et al., 2017, AJ, 154, 211
Kuncarayakti H. et al., 2018, A&A, 613, A35
Landolt A. U., 1992, AJ, 104, 340
Leloudas G. et al., 2015, A&A, 574, A61
Leonard D. C. et al., 2002, PASP, 114, 35
Lisakov S. M., Dessart L., Hillier D. J., Waldman R., Livne E., 2018, MNRAS, 473, 3863
Maguire K. et al., 2010, MNRAS, 404, 981
Marino R. A. et al., 2013, A&A, 559, A114
Maza J., Wischnjewsky M., Gonzalez L. E., 1983, IAUC Circ., 3827, 2
Meza N. et al., 2019, A&A, 629, A57
Minkowski R., 1941, PASP, 53, 224
Moriya T., Tominaga N., Blinnikov S. I., Baklanov P. V., Sorokina E. I., 2011, MNRAS, 415, 199
Moriya T. J., Yoon S.-C., Gräfener G., Blinnikov S. I., 2017, MNRAS, 469, L108
Moriya T. J., Förster F., Yoon S.-C., Gräfener G., Blinnikov S. I., 2018, MNRAS, 476, 2840
Morozova V., Piro A. L., Valenti S., 2017, ApJ, 838, 28
Morozova V., Piro A. L., Valenti S., 2018, ApJ, 858, 15
Mould J. R. et al., 2000, ApJ, 529, 786
Müller T., Prieto J. L., Pejcha O., Clocchiatti A., 2017, ApJ, 841, 127
Niemela V. S., Ruiz M. T., Phillips M. M., 1985, ApJ, 289, 52
Nugent P. et al., 2006, ApJ, 645, 841
Olivares E. F. et al., 2010, ApJ, 715, 833
Pastorello A. et al., 2006, MNRAS, 370, 1752
Pastorello A. et al., 2009, MNRAS, 394, 2266
Pejcha O., Prieto J. L., 2015, ApJ, 806, 225
Penston M. V., Blades J. C., 1980, MNRAS, 190, 51P
Persson S. E., Murphy D. C., Krzeminski W., Roth M., Rieke M. J., 1998, AJ, 116, 2475
Pettini M., Pagel B. E. J., 2004, MNRAS, 348, L59
Phillips M. M., Hamuy M., Maza J., Ruiz M. T., Carney B. W., Graham J. A., 1990, PASP, 102, 299
Phillips M. M. et al., 2013, ApJ, 779, 38
Pignata G. et al., 2009a, in Giobbi G., Tornambe A., Raimondo G., Limongi M., Antonelli L. A., Menci N., Brocato E., eds, AIP Conf. Proc., Vol. 1111, Probing Stellar Populations out to the Distant Universe: CEFALU 2008, Am. Inst. Phys., New York, p. 551
Pignata G. et al., 2009b, Cent. Bur. Electron. Telegrams, 1704, 1
Pignata G. et al., 2009c, Cent. Bur. Electron. Telegrams, 1719, 1
Polshaw J. et al., 2016, A&A, 588, A1
Poon H., Pun J. C. S., Lam T. Y., Qiu Y. L., Wei J. Y., 2011, preprint (arXiv:1109.0899)
Poznanski D., Prochaska J. X., Bloom J. S., 2012, MNRAS, 426, 1465
Pritchard T. A. et al., 2012, ApJ, 750, 128
Quimby R. M., Wheeler J. C., Höflich P., Akerlof C. W., Brown P. J., Rykoff E. S., 2007, ApJ, 666, 1093
Reichart D. et al., 2005, Nuovo Cimento C Geophys. Space Phys. C, 28, 767
Riess A. G. et al., 2016, ApJ, 826, 56
Rodríguez Ó., Clocchiatti A., Hamuy M., 2014, AJ, 148, 107
Rodríguez Ó. et al., 2019, MNRAS, 483, 5459
Roy R. et al., 2011, MNRAS, 414, 167
Saha A., Thim F., Tammann G. A., Reindl B., Sandage A., 2006, ApJS, 165, 108
Sahu D. K., Anupama G. C., Srividya S., Muneer S., 2006, MNRAS, 372, 1315
Sanders N. E. et al., 2015, ApJ, 799, 208
Schlafly E. F., Finkbeiner D. P., 2011, ApJ, 737, 103
Schlegel E. M., 1990, MNRAS, 244, 269
Schlegel D. J., Finkbeiner D. P., Davis M., 1998, ApJ, 500, 525
Shivvers I. et al., 2017, PASP, 129, 054201
Smith J. A. et al., 2002, AJ, 123, 2121
Smith N. et al., 2015, MNRAS, 449, 1876
Stritzinger M., Morrell N., 2008, Cent. Bur. Electron. Telegrams, 1329, 1
Stritzinger M., Morrell N., Folatelli G., Covarrubias R., Phillips M. M., 2009, Cent. Bur. Electron. Telegrams, 1725, 1
Szalai T. et al., 2019, ApJ, 876, 19
Taddia F. et al., 2013, A&A, 555, A10
Taddia F. et al., 2015, A&A, 580, A131
Takáts K. et al., 2015, MNRAS, 450, 3137
Tartaglia L. et al., 2020, A&A, 635, A39
Terreran G. et al., 2016, MNRAS, 462, 137
Thöne C. C. et al., 2017, A&A, 599, A129
Tomasella L. et al., 2013, MNRAS, 434, 1636
Tsvetkov D. Y., Pavlyuk N. N., 1997, Astron. Lett., 23, 26
Tsvetkov D. Y., Goranskij V., Pavlyuk N., 2008, Peremennye Zvezdy, 28, 8
Tsvetkov D. Y. et al., 2018, Astron. Lett., 44, 315
Tully R. B., Courtois H. M., Sorce J. G., 2016, AJ, 152, 50
Valenti S. et al., 2016, MNRAS, 459, 3939
Van Dyk S. D., Li W., Filippenko A. V., 2003, PASP, 115, 1289
Van Dyk S. D. et al., 2012, AJ, 143, 19
Van Dyk S. D. et al., 2019, ApJ, 875, 136
Vinkó J. et al., 2006, MNRAS, 369, 1780
Wang L., Strovink M., Conley A., Goldhaber G., Kowalski M., Perlmutter S., Siegrist J., 2006, ApJ, 641, 50
Woosley S. E., Pinto P. A., Martin P. G., Weaver T. A., 1987, ApJ, 318, 664
Yaron O. et al., 2017, Nat. Phys., 13, 510
Zhang T. et al., 2012, AJ, 144, 131

SUPPORTING INFORMATION

Supplementary data are available at *MNRAS* online.

Table A1. Optical magnitudes of the sequence stars in the field of SN 2008bm.
Table A2. Near-IR magnitudes of the sequence stars in the field of SN 2008bm.
Table A3. Optical magnitudes of the sequence stars in the field of SN 2009aj.
Table A4. Near-IR magnitudes of the sequence stars in the field of SN 2009aj.
Table A5. Optical magnitudes of the sequence stars in the field of SN 2009au.
Table A6. Near-IR magnitudes of the sequence stars in the field of SN 2009au.
Table A7. CSP-I photometry of SN 2008bm.
Table A8. Photometry of SN 2009aj.
Table A9. Photometry of SN 2009au.

Please note: Oxford University Press is not responsible for the content or functionality of any supporting materials supplied by the authors. Any queries (other than missing material) should be directed to the corresponding author for the article.

APPENDIX A: TABLES AND FIGURES

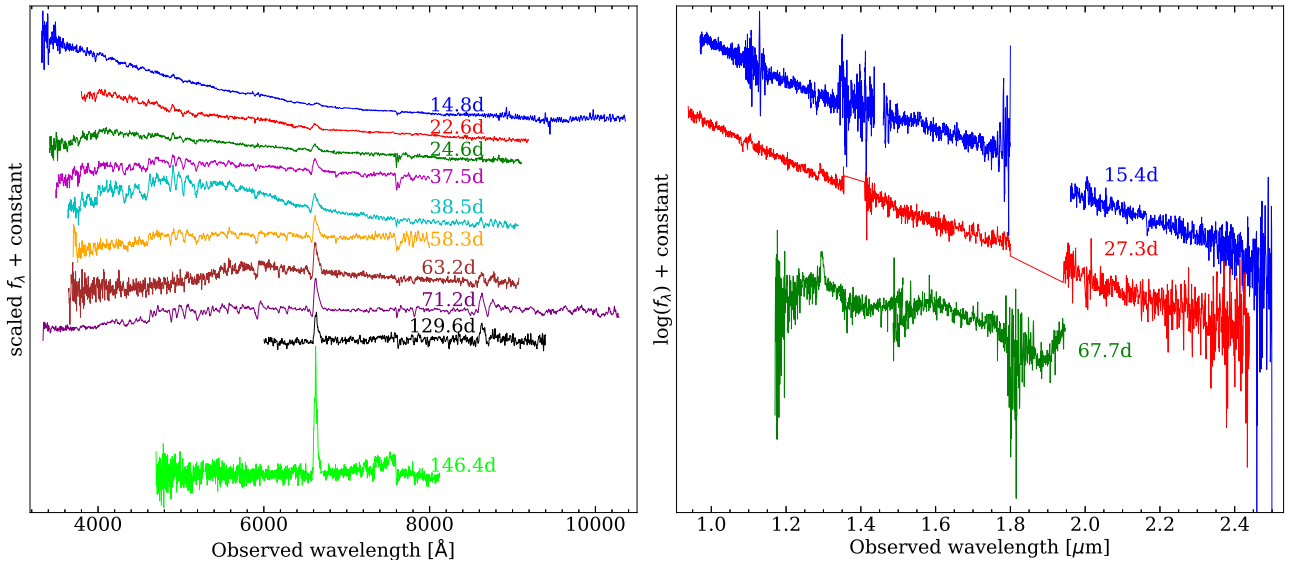

Figure A1. Left-hand panel: optical spectra of SN 2009au. Right-hand panel: near-IR spectra of SN 2009aj.

Table A1. Optical magnitudes of the sequence stars in the field of SN 2008bm. The full table is available online.

Star	α_{2000}	δ_{2000}	u (mag)	g (mag)	r (mag)	i (mag)	B (mag)	V (mag)
1	13:03:04.20	+10:28:43.0	–	–	–	14.570 (11)	15.606 (07)	14.907 (07)
2	13:02:56.57	+10:29:47.3	16.667 (25)	15.587 (12)	15.120 (03)	14.938 (09)	15.918 (08)	15.311 (07)
3	13:02:50.77	+10:31:10.4	16.569 (50)	15.497 (50)	15.498(41)	15.567 (17)	15.763 (85)	15.490 (56)

Note. Errors, in parenthesis and in units of 0.001 mag, are 1σ.

Table A2. Near-IR magnitudes of the sequence stars in the field of SN 2008bm. The full table is available online.

Star	α_{2000}	δ_{2000}	Y (mag)	J (mag)	H (mag)
1	13:03:16.69	+10:33:09.6	13.140 (18)	12.883 (29)	12.492 (09)
2	13:02:55.18	+10:28:25.5	13.215 (14)	12.788 (34)	12.072 (32)
3	13:03:05.57	+10:26:33.2	13.459 (14)	13.071 (34)	12.461 (35)

Note. Errors, in parenthesis and in units of 0.001 mag, are 1σ.

Table A3. Optical magnitudes of the sequence stars in the field of SN 2009aj. The full table is available online.

Star	α_{2000}	δ_{2000}	u (mag)	g (mag)	r (mag)	i (mag)	z (mag)	U (mag)	B (mag)	V (mag)	R (mag)	I (mag)
1	13:56:26.43	–48:31:56.8	–	–	–	13.978 (15)	–	–	14.989 (32)	14.316 (31)	–	–
2	13:57:02.68	–48:30:11.4	–	–	–	13.775 (15)	13.739 (40)	–	15.109 (25)	14.259 (27)	–	–
3	13:56:55.56	–48:33:32.8	–	–	–	14.081 (03)	14.103 (42)	–	15.127 (25)	14.422 (29)	–	–

Note. Errors, in parenthesis and in units of 0.001 mag, are 1σ.

Table A4. Near-IR magnitudes of the sequence stars in the field of SN 2009aj. The full table is available online.

Star	α_{2000}	δ_{2000}	Y (mag)	J (mag)	H (mag)
1	13:56:56.40	−48:29:39.5	12.653 (10)	12.400 (10)	12.092 (11)
2	13:56:47.70	−48:33:36.7	12.501 (06)	12.189 (07)	11.754 (07)
3	13:56:43.43	−48:25:06.7	13.101 (07)	12.896 (12)	12.648 (18)

Note. Errors, in parenthesis and in units of 0.001 mag, are 1σ.

Table A5. Optical magnitudes of the sequence stars in the field of SN 2009au. The full table is available online.

Star	α_{2000}	δ_{2000}	u (mag)	g (mag)	r (mag)	i (mag)	z (mag)	B (mag)	V (mag)	R (mag)	I (mag)
1	12:59:31.60	−29:32:03.1	16.470 (35)	15.097 (22)	14.621 (11)	14.400 (21)	14.327 (20)	15.513 (30)	14.801 (26)	14.414 (22)	13.983 (22)
2	12:59:51.12	−29:37:51.5	17.176 (107)	15.316 (26)	14.694 (11)	14.437 (22)	14.329 (16)	15.805 (25)	14.931 (22)	14.467 (26)	14.000 (26)
3	12:59:38.00	−29:32:02.3	16.256 (48)	14.940 (24)	14.483 (11)	14.236 (09)	14.155 (18)	15.349 (27)	14.654 (25)	14.279 (24)	13.822 (24)

Note. Errors, in parenthesis and in units of 0.001 mag, are 1σ.

Table A6. Near-IR magnitudes of the sequence stars in the field of SN 2009au. The full table is available online.

Star	α_{2000}	δ_{2000}	Y (mag)	J (mag)	H (mag)
1	13:00:04.82	−29:38:23.8	12.453 (21)	11.976 (15)	11.317 (09)
2	13:00:10.53	−29:35:09.2	12.587 (22)	12.206 (18)	11.675 (12)
3	12:59:47.94	−29:39:32.1	12.863 (17)	12.596 (14)	12.309 (09)

Note. Errors, in parenthesis and in units of 0.001 mag, are 1σ.

Table A7. CSP-I photometry of SN 2008bm. The full table is available online.

MJD	u (mag)	g (mag)	r (mag)	i (mag)	B (mag)	V (mag)	Y (mag)	J (mag)	H (mag)
54558.23	18.548 (24)	17.701 (09)	17.536 (08)	17.579 (12)	17.945 (10)	17.763 (10)	–	–	–
54559.34	–	–	–	–	–	–	17.257 (15)	17.125 (21)	17.096 (59)
54560.25	18.755 (32)	17.757 (08)	17.584 (08)	17.602 (09)	18.023 (11)	17.764 (09)	–	–	–

Note. Errors, in parenthesis and in units of 0.001 mag, are 1σ.

Table A8. Photometry of SN 2009aj. The full table is available online.

MJD	u (mag)	g (mag)	r (mag)	i (mag)	z (mag)	U (mag)	B (mag)	V (mag)	R (mag)	I (mag)	Y (mag)	J (mag)	H (mag)	Telescope
54873.20	–	–	–	–	–	–	–	>18.412[a]	–	–	–	–	–	PROMPT
54886.26	–	–	–	–	–	–	–	15.631 (29)[a]	–	–	–	–	–	PROMPT
54888.18	–	–	–	–	–	–	–	15.417 (31)[a]	–	–	–	–	–	PROMPT

Notes. Errors, in parenthesis and in units of 0.001 mag, are 1σ.
[a]Unfiltered photometry calibrated to the V band.

Table A9. Photometry of SN 2009au. The full table is available online.

MJD	u (mag)	g (mag)	r (mag)	i (mag)	z (mag)	B (mag)	V (mag)	R (mag)	I (mag)	Y (mag)	J (mag)	H (mag)	Telescope
54886.18	–	–	–	–	–	–	>19.042[a]	–	–	–	–	–	PROMPT
54893.15	–	–	–	–	–	–	>17.656[a]	–	–	–	–	–	PROMPT
54901.17	–	–	–	–	–	–	17.629 (77)[a]	–	–	–	–	–	PROMPT

Notes. Errors, in parenthesis and in units of 0.001 mag, are 1σ.
[a]Unfiltered photometry calibrated to the V band.

Table A10. Optical spectroscopy of SN 2009au.

UT date	MJD	Phase[a] (d)	Instrument setup[b]	Wavelength range (Å)	Exposure time (s)	Slit (arcsec)
2009-03-22	54912.11	14.8	TNG+LRS (+LR-B, LR-R)	3320–10360	1200, 1200	1.5
2009-03-30	54920.03	22.6	TNG+LRS (+LR-B, LR-R)	3800–9190	1800, 1800	1.5
2009-04-01	54922.05	24.6	NOT+ALFOSC (+gm4)	3420–9110	900	1.0
2009-04-14	54935.04	37.5	NOT+ALFOSC (+gm4)	3490–8000	1200	1.0
2009-04-15	54936.05	38.5	NOT+ALFOSC (+gm4)	3640–9070	2700	1.3
2009-05-05	54956.01	58.3	NOT+ALFOSC (+gm4)	3700–8000	1800	1.0
2009-05-09	54960.99	63.2	NOT+ALFOSC (+gm4)	3640–9080	900	1.3
2009-05-18	54969.13	71.2	NTT+EFOSC (+gr11)	3340–10290	1200	1.0
2009-07-16	55028.08	129.6	NTT+EFOSC (+gr16)	6000–9400	2400	1.5
2009-08-01	55044.98	146.4	Gemini-S+GMOS (+R400)	4700–8120	1800	1.0

[a]Since explosion (MJD 54897.2).
[b]TNG+LRS: 3.58-m Telescopio Nazionale Galileo (La Palma, Spain) + Low Resolution Spectrograph; NOT+ALFOSC: 2.56-m Nordic Optical Telescope (La Palma, Spain) + Alhambra Faint Object Spectrograph and Camera; NTT+EFOSC: 3.58-m New Technology Telescope (La Silla, Chile) + ESO Faint Object Spectrograph and Camera; Gemini-S+GMOS: 8.1-m Gemini South Telescope (Cerro Pachón, Chile) + Gemini Multi-Object Spectrograph.

Table A11. Near-IR spectroscopy of SN 2009aj.

UT date	MJD	Phase[a] (d)	Instrument setup[b]	Wavelength range (Å)	Exposure time (s)	Slit (arcsec)
2009-03-04	54895.38	15.4	VLT+ISAAC (+SWS1-LR)	9700–25000	600	1.0
2009-03-16	54907.36	27.3	NTT+SOFI (+GB, GR)	9400–24400	2700, 5400	0.6
2009-04-26	54948.17	67.7	SOAR+OSIRIS (+LR)	11700–19400	2400, 2400	1.0

[a]Since explosion (MJD 54879.8).
[b]VLT+ISAAC: 8.2-m Very Large Telescope UT1 (Paranal, Chile) + Infrared Spectrometer And Array Camera; NTT+SOFI: 3.58-m New Technology Telescope (La Silla, Chile) + Son of ISAAC; SOAR+OSIRIS: 4.1-m Southern Astrophysical Research Telescope (Cerro Pachón, Chile) + Ohio State Infrared Imager/Spectrometer.

Table A12. SN and host galaxy parameters of the SN IIn/II sample.

SN data	1979C	1998S	2007pk	2008fq	PTF11iqb	2013fc
Host galaxy	M100	NGC 3877	NGC 579	NGC 6907	NGC 151	ESO 154-G10
Host type[a]	SAB(s)bc	SA(s)c?	Scd?	SB(s)bc	SB(r)bc	(R')SB(r)a?
$E^{\rm MW}_{B-V}$ (mag)[b]	0.023	0.020	0.045	0.055	0.028	0.026
$E^{\rm host}_{B-V}$ (mag)	$0.13^{+0.06}_{-0.02}$	$0.20^{+0.11}_{-0.08}$	0.09 ± 0.04[c]	0.99 ± 0.14[d]	0.0	0.91 ± 0.06
Explosion epoch (MJD)	43970.4 ± 8.4	50871.2 ± 3.5	54411.8 ± 2.5	54719.8 ± 4.5	55762.2 ± 2.7	56516.2 ± 2.0
$cz_{\rm helio}$ (km s^{-1})[a, e]	1571	895	4993	3182	3747	5586
μ_z (mag)[f]	30.74 ± 0.81	31.24 ± 0.64	34.14 ± 0.17	33.37 ± 0.24	33.51 ± 0.23	34.43 ± 0.15
$\mu_{z{\rm i}}$ (mag)[g]	31.18 ± 0.05[‡]	30.92 ± 0.45[†]	–	32.80 ± 0.40[†]	33.89 ± 0.40[†]	–
Adopted μ (mag)[h]	31.18 ± 0.05	31.03 ± 0.37	34.14 ± 0.17	33.22 ± 0.21	33.60 ± 0.21	34.43 ± 0.15
12+log(O/H) (dex)[i]	–	8.56 ± 0.10[⋆]	8.42 ± 0.04[◇]	8.57 ± 0.04[⊗]	8.61 ± 0.03[⋆]	8.55 ± 0.04[⊕]
s_2 (mag (100 d)$^{-1}$)	3.05 ± 0.08	3.62 ± 0.09	2.28 ± 0.05	1.77 ± 0.08	1.40 ± 0.10	3.59 ± 0.12
$M_V^{\rm max}$ (mag)	-19.55 ± 0.14	-19.46 ± 0.49	-18.54 ± 0.21	-20.82 ± 0.50	-18.34 ± 0.23	-20.13 ± 0.24
$M_V^{\rm 50d}$ (mag)	-18.26 ± 0.31	-18.39 ± 0.49	-17.64 ± 0.21	-19.78 ± 0.50	-17.39 ± 0.25	-18.85 ± 0.24
^{56}Ni mass ($M_\odot$)	$>0.069 \pm 0.010$[j]	$>0.155 \pm 0.069$[j]	–	–	0.029 ± 0.007	$>0.279 \pm 0.070$[j]
$(B-V)_{\rm 50d}$ (mag)	0.53 ± 0.05	0.40 ± 0.11	0.69 ± 0.09	0.51 ± 0.14	0.46 ± 0.07	0.42 ± 0.16
pEW$^{\rm 50d}_{\rm FeII\lambda5018}$ (Å)	8.03 ± 0.40	9.68 ± 0.31	11.49 ± 0.14	14.09 ± 0.46	–	14.78 ± 0.98

Table A12 – *continued*

SN data	1979C	1998S	2007pk	2008fq	PTF11iqb	2013fc
$v_{\rm FeII}^{\rm 50d}$ (km s^{-1})	6086 ± 315	4355 ± 183	5086 ± 185	5365 ± 228	–	5682 ± 196
References[k]	1, 2, 3, 4, 5	6, 7, 8	9, 10	11, 12	13	14

[a]From NED.
[b]Galactic colour excesses from Schlafly & Finkbeiner (2011), with a statistical uncertainty of 16 per cent (Schlegel et al. 1998).
[c]Average of the $E_{B-V}^{\rm host}$ values reported in Pritchard et al. (2012) and Inserra et al. (2013).
[d]SN 2008fq has a Na I D pEW of 2.9 ± 0.2 Å (Taddia et al. 2013), which is unhelpful to estimate $E_{B-V}^{\rm host}$ (see Section 2.3). As for SN 2009au, we compute $E_{B-V}^{\rm host}$ matching the $B-V$ colour curve of SN 2008fq to the rest of SNe IIn/II.
[e]Heliocentric velocities, with an error of 162 km s^{-1} to take into account the host galaxy rotational velocity (Anderson et al. 2014a).
[f]Distance moduli computed from recessional velocities, corrected for the infall of the Local Group towards the Virgo cluster and the great attractor (Mould et al. 2000), and assuming $H_0 = 73$ km s^{-1} Mpc^{-1}. We include an error of 382 km s^{-1} due to peculiar velocities (Wang et al. 2006).
[g]Redshift-independent distance moduli (when available): (‡) Cepheids distance from Saha et al. (2006); (†) Tully–Fisher distance from the extragalactic distance database (EDD, http://edd.ifa.hawaii.edu/).
[h]Weighted average of μ_z and μ_{zi} (if it is available). For SN 1979C, we adopt the Cepheid distance modulus.
[i]Oxygen abundances, in the N2 calibration of Marino et al. (2013), measured by Anderson et al. (2016) (⊗), Taddia et al. (2015) (⋆), Inserra et al. (2013) (⋄), and Kangas et al. (2016) (⊕). The latter three are recalibrations of the original values reported in the N2 calibration of Pettini & Pagel (2004).
[i] ^{56}Ni masses measured with the Hamuy (2003) relation and BC = 0.26 ± 0.06 (Hamuy 2001). The upper limits are because the slope during the radioactive tail is >1.5 mag (100 d)$^{-1}$.
[j] Since $s_3 > 1.5$ mag (100 d)$^{-1}$, ^{56}Ni mass estimations are lower limits.
[k](1) Balinskaia et al. (1980); (2) de Vaucouleurs et al. (1981); (3) Branch et al. (1981); (4) Barbon et al. (1982); (5) Penston & Blades (1980); (6) Fassia et al. (2000); (7) Poon et al. (2011); (8) Fassia et al. (2001); (9) Inserra et al. (2013); (10) Hicken et al. (2017); (11) Taddia et al. (2013); (12) Faran et al. (2014); (13) Smith et al. (2015); and (14) Kangas et al. (2016).

Table A13. Properties of the normal SNe II with $B-V$ colours during the radioactive tail.

SN	t_0 (MJD)	$E_{B-V}^{\rm MW}$† (mag)	$E_{B-V}^{\rm host}$ (mag)	$cz_{\rm helio}^{\ddagger}$ (km s^{-1})	Ref*	SN	t_0 (MJD)	$E_{B-V}^{\rm MW}$† (mag)	$E_{B-V}^{\rm host}$ (mag)	$cz_{\rm helio}^{\ddagger}$ (km s^{-1})	Ref*
1969L	40550.0 ± 5.0	0.053	0.000 ± 0.097	518	1, 2	2007it	54348.0 ± 1.0	0.099	0.019 ± 0.013	1193	15, 16
1992H	48660.5 ± 10.0	0.015	0.000 ± 0.097	1793	2, 3	2008bk	54540.9 ± 8.0	0.017	0.000 ± 0.016	230	7, 16, 17
1996W	50179.5 ± 3.0	0.036	0.187	1617	4	2008gz	54693.5 ± 5.0	0.036	0.030 ± 0.040	1862	18
1999ca	51277.5 ± 7.0	0.094	0.039 ± 0.100	2791	5, 6, 7	2009bw	54916.0 ± 3.0	0.197	0.080	1155	19
1999em	51475.2 ± 3.8	0.035	0.100 ± 0.052	800	5, 6, 8	2012A	55928.7 ± 4.7	0.027	0.009	753	20
2003B	52621.7 ± 4.3	0.023	0.000 ± 0.081	1141	5, 6	2012aw	56002.1 ± 0.8	0.024	0.046 ± 0.008	778	21, 22
2003gd	52715.0 ± 3.0	0.060	0.130 ± 0.100	657	5, 6, 9	2014cx	56901.9 ± 0.5	0.096	0.0	1646	23
2004dj	53186.5 ± 3.0	0.034	0.161 ± 0.081	221	6, 10, 11	ASAS14jb	56945.6 ± 3.0	0.015	0.0	1808	24
2004et	53270.5 ± 0.5	0.293	0.000 ± 0.081	40	6, 12	ASAS15oz	57261.1 ± 4.0	0.078	0.0	2078	25
2005cs	53548.4 ± 0.5	0.032	0.040 ± 0.050	463	13, 14	2017eaw	57886.2 ± 1.0	0.293	0.0	40	26, 27, 28

†Galactic colour excesses from Schlafly & Finkbeiner (2011), with a statistical error of 16 per cent (Schlegel et al. 1998).
‡Heliocentric redshifts from NED.
*References: (1) Ciatti, Rosino & Bertola (1971); (2) Hamuy (2003); (3) Clocchiatti et al. (1996); (4) Inserra et al. (2013); (5) Galbany et al. (2016); (6) Olivares E. et al. (2010); (7) G17; 8) Elmhamdi et al. (2003); (9) Van Dyk, Li & Filippenko (2003); (10) Vinkó et al. (2006); (11) Tsvetkov, Goranskij & Pavlyuk (2008); (12) Maguire et al. (2010); (13) Pastorello et al. (2009); (14) Dessart et al. (2008); (15) Andrews et al. (2011); (16) Anderson et al. (2014b); (17) Van Dyk et al. (2012); (18) Roy et al. (2011); (19) Inserra et al. (2012); (20) Tomasella et al. (2013); (21) Bose et al. (2013); (22) Dall'Ora et al. (2014); (23) Huang et al. (2016); (24) Meza et al. (2019); (25) Bostroem et al. (2019); (26) Tsvetkov et al. (2018); (27) Szalai et al. (2019); and (28) Van Dyk et al. (2019).

Table A14. Properties and references of the SNe IIn used in this work.

SN	t_0 (MJD)	$E_{B-V}^{\rm MW}$† (mag)	$E_{B-V}^{\rm host}$ (mag)	$cz_{\rm helio}^{\ddagger}$ (km s^{-1})	References*
1994Y	49570.1 ± 5.9	0.008	0.0	2558	1, 2
1996al	50255.0 ± 2.0	0.010	0.10 ± 0.05	1970	3
2010jl	55473.5 ± 5.0	0.023	0.02	3214	4, 5
2011ht	55833.2	0.072	0.0	1093	6
2015bh	57154.8 ± 3.9	0.019	0.21 ± 0.07	1947	7, 8
2015da	57030.4 ± 1.5	0.012	0.97 ± 0.27	2165	9

†Galactic colour excesses from Schlafly & Finkbeiner (2011), with a statistical error of 16 per cent (Schlegel et al. 1998).
‡Heliocentric redshifts from NED.
*(1) Ho et al. (2001); (2) Tsvetkov & Pavlyuk (1997); (3) Benetti et al. (2016); (4) Fransson et al. (2014); (5) Chandra et al. (2015); (6) Humphreys et al. (2012); (7) Elias-Rosa et al. (2016); (8) Thöne et al. (2017); and (9) Tartaglia et al. (2020).

Table A15. New estimation of the nickel masses for the SNe II in the Hamuy sample.

SN⋆	$E_{B-V}^{\rm MW}$ † (mag)	$E_{B-V}^{\rm host}$ ∗ (mag)	$\mu_z^{\diamond}$ (mag)	$\mu_{zi}^{\oslash}$ (mag)	$\mu^{\ddagger}$ (mag)	$M_V^{50\rm d}$ (mag)	$M(^{56}\rm Ni)$ ($\rm M_{\odot}$)
1969L	0.053	0.000 ± 0.097^a	29.78 ± 1.26	29.84 ± 0.04^c	29.84 ± 0.04	-16.65 ± 0.31	0.068 ± 0.021
1970G	0.008	0.000 ± 0.097^a	28.96 ± 1.83	29.14 ± 0.05^d	29.14 ± 0.05	-17.06 ± 0.34	0.030 ± 0.010
1973R	0.028	0.452 ± 0.097^a	29.07 ± 1.74	30.18 ± 0.04^e	30.18 ± 0.04	-17.11 ± 0.31	0.093 ± 0.036
1986I	0.034	0.065 ± 0.097^a	33.00 ± 0.29	30.71 ± 0.40^f	30.71 ± 0.40	-16.47 ± 0.54	0.076 ± 0.036
1988A	0.035	0.000 ± 0.097^a	30.71 ± 0.82	31.11 ± 0.40^f	31.03 ± 0.36	-16.14 ± 0.47	0.054 ± 0.027
1990E	0.022	0.468 ± 0.097^a	31.07 ± 0.69	30.89 ± 0.45^f	30.94 ± 0.38	-16.56 ± 0.52	0.044 ± 0.022
1990K	0.012	0.065 ± 0.097^a	31.66 ± 0.53	31.82 ± 0.45^f	31.75 ± 0.34	-17.49 ± 0.50	0.036 ± 0.017
1991G	0.017	0.000 ± 0.097^a	30.90 ± 0.75	30.64 ± 0.45^f	30.71 ± 0.39	-15.23 ± 0.50	0.020 ± 0.009
1992H	0.015	0.000 ± 0.097^a	32.53 ± 0.35	32.23 ± 0.45^f	32.42 ± 0.28	-17.48 ± 0.41	0.139 ± 0.054
1992ba	0.050	0.139 ± 0.052^b	30.76 ± 0.80	–	30.76 ± 0.80	-15.92 ± 0.82	0.024 ± 0.018
1999gi	0.014	0.181 ± 0.052^b	30.01 ± 1.13	30.77 ± 0.06^c	30.77 ± 0.06	-16.47 ± 0.18	0.041 ± 0.007

Note. To recompute $M_V^{50\,\rm d}$ and $M(^{56}\rm Ni)$, we use the same observables listed in table 2 of Hamuy (2003).

⋆We recompute $M_V^{50\,\rm d}$ and $M(^{56}\rm Ni)$ values only for the SNe that do not have $M(^{56}\rm Ni)$ estimations in the A14 sample, with three or more V-band photometric points during the nebular phase, and with $s_3 < 1.3$ mag $(100\,\rm d)^{-1}$.

†Galactic colour excesses from Schlafly & Finkbeiner (2011), with a statistical error of 16 per cent (Schlegel et al. 1998).

∗Host galaxy reddening values from Hamuy (2003) (a) or Olivares E. et al. (2010) (b).

$^{\diamond}$Distance moduli computed from recessional velocities, corrected for the infall of the Local Group towards the Virgo cluster and the Great Attractor (Mould et al. 2000), and assuming $H_0 = 73\ \rm km\,s^{-1}\,Mpc^{-1}$. We include an error of 382 $\rm km\,s^{-1}$ due to peculiar velocities (Wang et al. 2006).

$^{\oslash}$Redshift-independent distance moduli: Cepheid distance from Saha et al. (2006) (c) and Riess et al. (2016) (d); TRGB distance from Jang & Lee (2017) (e); Tully–Fisher distance from EDD (f). We do not consider distances computed with the SN itself.

‡Weighted average of μ_z and μ_{zi} (if it is available). For SN 1969L, SN 1970G, SN 1973R, SN 1986I, and SN 1999gi, we adopt the redshift-independent distance modulus.

[1]*Departamento de Ciencias Fisicas, Universidad Andres Bello, Avda. Republica 252, Santiago, Chile*
[2]*Millennium Institute of Astrophysics (MAS), Nuncio Monseñor Sotero Sanz 100, Providencia, Santiago, Chile*
[3]*School of Physics and Astronomy, Tel Aviv University, Tel Aviv 69978, Israel*
[4]*European Southern Observatory, Alonso de Córdova 3107, Casilla 19, Santiago, Chile*
[5]*Division of Science, National Astronomical Observatory of Japan, National Institutes of Natural Sciences, 2-21-1 Osawa, Mitaka, Tokyo 181-8588, Japan*
[6]*School of Physics and Astronomy, Faculty of Science, Monash University, Clayton, VIC 3800, Australia*
[7]*Instituto de Astrofísica, Pontificia Universidad Católica de Chile, Av. Vicuña Mackenna 4860, 782-0436 Macul, Santiago, Chile*
[8]*Center for Mathematical Modeling, University of Chile, Beaucheff 851, 7th floor, Santiago, Chile*
[9]*Núcleo de Astronomía de la Facultad de Ingeniería y Ciencias, Universidad Diego Portales, Av. Ejército 441, Santiago, Chile*
[10]*Carnegie Observatories, Las Campanas Observatory, Casilla 60, La Serena, Chile*
[11]*Observatories of the Carnegie Institution for Science, 813 Santa Barbara Street, Pasadena, CA 91101, USA*
[12]*Instituto de Astrofísica de La Plata (IALP), CONICET, Paseo del Bosque S/N, B1900FWA La Plata, Argentina*
[13]*Facultad de Ciencias Astronómicas y Geofísicas, Universidad Nacional de La Plata, Paseo del Bosque, B1900FWA, La Plata, Argentina*
[14]*Kavli Institute for the Physics and Mathematics of the Universe, Todai Institutes for Advanced Study, University of Tokyo, 5-1-5 Kashiwanoha, Kashiwa, Chiba 277-8583, Japan*
[15]*Department of Physics and Astronomy, University of Southampton, Southampton SO17 1BJ, UK*
[16]*Departamento de Astronomía, Universidad de Chile, Casilla 36-D, Santiago, Chile*
[17]*Department of Physics and Astronomy, Aarhus University, Ny Munkegade 120, DK-8000 Aarhus C, Denmark*
[18]*George P. and Cynthia Woods Mitchell Institute for Fundamental Physics and Astronomy, Texas A&M University, College Station, TX 77843, USA*
[19]*INAF – Osservatorio Astronomico di Padova, Vicolo dell'Osservatorio 5, I-35122 Padova, Italy*
[20]*Cerro Tololo Inter-American Observatory, National Optical Astronomy Observatory, Casilla 603, La Serena, Chile*
[21]*Department of Physics and Astronomy, University of North Carolina at Chapel Hill, Campus Box 325, Chapel Hill, NC 27599, USA*

This paper has been typeset from a TEX/LATEX file prepared by the author.